Three-dimensional pathways of dust over the Sahara during summertime 2011 as revealed by new IASI observations

Juan Cuesta[1*], Cyrille Flamant[2], Marco Gaetani[2,3], Peter Knippertz[4], Andreas H. Fink[4], Patrick Chazette[5], Maxim Eremenko[1], Gaëlle Dufour[1], Claudia Di Biagio[1] and Paola Formenti[1]

(1) Laboratoire Interuniversitaire des Systèmes Atmosphériques, UMR CNRS 7583, Université Paris Est Créteil, Université de Paris, Créteil, France

(2) Laboratoire Atmosphères, Milieux, Observations Spatiales, UMR CNRS 8190, Sorbonne Université, Université Versailles Saint Quentin, Paris, France

(3) Scuola Universitaria Superiore IUSS, Pavia, Italy

(4) Karlsruher Institut für Technologie, Institut für Meteorologie und Klimaforschung, Karlsruhe, Germany

(5) Laboratoire des Sciences du Climat et de l'Environnement, UMR CNRS 8212, Université Versailles Saint Quentin, Saclay, France

*Corresponding author:

Juan Cuesta

Phone: 33 (0) 1 82 39 20 64

E-mail : cuesta@lisa.u-pec.fr

This article has been accepted for publication and undergone full peer review but has not been through the copyediting, typesetting, pagination and proofreading process which may lead to differences between this version and the Version of Record. Please cite this article as doi: 10.1002/qj.3814

Abstract

We present a new characterization of the three-dimensional (3D) distribution of dust over the Sahara during summertime, exemplarily for June 2011. Our approach called AEROIASI is based on the innovative retrieval of vertical profiles of dust extinction coefficient from daily cloud-free hyperspectral satellite observations of IASI (Infrared Atmospheric Sounder Interferometer). AEROIASI observations clearly agree with other widely used measurements (from lidar and radiometers).

The 3D characterisation is focused on the dust maximum in June 2011, located in the central Sahara (17–23°N 1–7°E), and linked with the major atmospheric dynamical drivers associated with the West African Monsoon (WAM) system. AEROIASI shows near-surface dust load to be dominated by five major emission events occurring every 3–4 days. All these occur when the study region is under the influence of northward bursts of the WAM and convection-related cold pools, likely associated with orographic forcing by the Aïr Mountains. During the earliest (10 June) and the dustiest (17 June) cases, northward advection of moisture over the hot spot is favoured by the superposition of cyclonic circulations related to an extra-topical disturbance northwest of the Sahara and to the Saharan heat low over Mauritania, respectively. Convection over the hot spot also triggers wave-like disturbances that travel westwards. The three dustiest events are characterised by elongated dust fronts moving northwards, with a leading edge spanning 200–300 km horizontally and extending from the surface up to 2 km of altitude. Farther south the dust layer progressively elevates to 3.5 km along the slanted isentropes at the interface of the monsoon and the harmattan, increasingly losing contact with the ground. When northerlies blow over the study region, elevated dust layers at 3–5 km are observed, which are transported southwards within the Saharan air layer and westwards along the northern edge of the African easterly jet (after 13 June).

Keywords: dust vertical profile, West African monsoon bursts, cold pools, haboobs

1. Introduction

Desert dust plays a major role in the Earth system (e.g. Mahowald et al., 2001; Yoshioka et al., 2007; Knippertz and Stuut, 2014). In terms of mass concentration, it is one of the most abundant aerosol species in the atmosphere (e.g. Heald et al., 2014). The life cycle of desert dust and its numerous environmental impacts are closely related to its three-dimensional (3D) spatial distribution. Once uplifted from the surface over source regions, dust is transported to remote regions by the atmospheric circulation (e.g. Yu et al., 2012; Guo et al., 2019; Lieu et al., 2019). Depending on the altitudes at which it is transported, dust impacts differ dramatically on the Earth radiative budget (e.g. Haywood and Boucher, 2000; Meloni et al., 2005), atmospheric stability (e.g. Jones et al., 2004; Dunion and Velden, 2004), cloud properties (e.g. Bangert et al., 2012) as well as chemical (e.g. Su et al., 2010) and biogeochemical (e.g. Mahowald et al., 2005) processes. When transported near the surface, dust causes poor air quality, low visibility and deposits on the ground (e.g. Xu et al., 1994; Prospero, 1999; Mahowald et al., 2007). Therefore, accurate knowledge of the 3D pathways of desert dust transport and the associated dynamical processes is fundamental for assessing its major impacts on the environment.

The Sahara is the world's largest source of dust aerosols. Dust emissions and transport within and beyond this region are driven by multiple dynamical mechanisms from micro to synoptic scales. Large amounts of dust are lifted after sunrise by strong near-surface winds associated with north-easterly dry harmattan flow enhanced by vertical mixing of the nocturnal low-level jet (LLJ) momentum down to the surface (e.g. Washington and Todd, 2005; Lothon et al., 2008; Knippertz, 2008). Near the surface, these winds encounter the south-westerly moist West African monsoon (WAM) flow at the inter-tropical discontinuity (ITD, see the schematic in Fig. 1), which is located over the Sahel from April to June e.g. (Bock et al., 2008; Guichard et al., 2009; Couvreux et al., 2009; Lele and Lamb, 2010) and at the southern fringes of the Sahara in July and August e.g. (Sultan and Janicot, 2000, 2003; Cuesta et al., 2009). The winds at the leading edge of the WAM flow can act to uplift dust e.g. (Flamant et al., 2007; Bou Karam et al., 2008). Moreover, mesoscale convective systems (MCS) travelling across the Sahel during the summer often generate cold pools that propagate rapidly over long distances and lift substantial amounts of dust (Knippertz et al., 2007; Marsham et al., 2008; Flamant et al., 2009; Roberts and Knippertz, 2012). The cold pools related dust storms are also called haboobs and have a density-current like appearance (e.g. Knippertz and Stuut, 2014). Orography is also known to trigger convection that lead to the generation of haboobs, as found over the Atlas (Knippertz et al., 2007), as well as the Hoggar and Aïr Mountains (Roberts and Knippertz, 2014). Other key dynamical actors of this region are the African easterly waves (AEWs) propagating along the African

easterly jet (AEJ) within the 10–20°N latitudinal band (with typical periods of 3 to 5 days and detected at 700–850 hPa, e.g. Fink and Reiner, 2003). Knippertz and Todd (2010) showed that AEWs in concert with extratropical disturbances substantially contribute to the generation of a major dust hotspot over eastern Mauritania and northern Mali, through both emission and organization of transport. Dust over this region is often uplifted by cold pools generated by convection associated with southerly moisture advection behind AEW troughs. Northerlies ahead of AEW troughs transport dust over the hotspot in the upper parts of the deep Saharan boundary layer (Chaboureau et al., 2016). The top of the boundary layer over the central Sahara may typically reach altitudes up to 5 to 6 km during summer (e.g. Cuesta et al., 2008, 2009).

Due to a lack of routine ground-based measurements over the Sahara, satellite observations play a central role in describing the spatial distribution of dust. At the daily scale, almost all satellite observations only provide two-dimensional (2D) information of the dust distribution. Indeed, this is done either in terms of the horizontal distribution of aerosol optical depth (AOD) typically derived by MODIS (Moderate-resolution Image Spectroradiometer, Remer et al., 2005; Sayer et al., 2013) and OMI (Ozone Monitoring Instrument, Torres et al., 2007) , or vertical transects of the aerosol distribution along defined tracks measured by the space-borne lidars LITE (Lidar in-Space Technology Experiment, Berthier et al., 2006) and CALIOP (Cloud-Aerosol Lidar with Orthogonal Polarization) onboard CALIPSO (Cloud-Aerosol Lidar and Infrared Pathfinder Satellite Observations, Winker et al., 2007). However, tracking the evolution of the dust vertical distribution with a space-borne lidar alone at daily scale is difficult, since daytime or night-time transects are longitudinally spaced by large distances (around 2000 km for CALIOP) in mid-latitudes and the Tropics and the ground footprint is narrow (90 m width for CALIOP).

Thermal infrared passive instruments as the High-Resolution Infrared Radiation Sounder (HIRS-2) have been shown to be relevant to assess both the vertical distribution and the optical thickness of aerosols, mainly in the stratosphere (Pierangelo et al., 2004). More recently, hyperspectral sounders have shown the capability for deriving the vertical distribution of desert dust. Daily observations of the top and mean heights of Saharan dust plumes have been derived respectively from AIRS (Atmospheric Infrared Sounder) (DeSouza-Machado et al., 2010) and IASI (Infrared Atmospheric Spectral Interferometer) (Kylling et al., 2018). Vertical profiles of dust load have been derived from IASI, firstly over ocean and with limited coverage over land (Vandenbussche et al., 2013) and more recently over both land and ocean (Cuesta et al., 2015; Callewaert et al., 2019). Moreover, IASI measurements have allowed the first 3D observation of both the vertical distribution and the horizontal structure of dust plumes with full coverage for cloud-free conditions, on a daily basis and over all

surfaces (both over land and ocean) using the so-called AEROIASI approach (Cuesta et al. 2015). AEROIASI uses the hyperspectral measurements of IASI to derive vertically resolved horizontal fields of the aerosol extinction coefficient at 10 µm for cloud-free conditions. Previous studies using AEROIASI observations of the 3D distribution of dust were focused on East Asia (Cuesta et al., 2015) and the middle East (Francis et al., 2019). For these studies, a remarkable agreement between AEROIASI and CALIOP was found for several transects of vertical profiles of the major dust plumes.

In the present paper, we use the AEROIASI approach to conduct the first observational study of the 3D distribution of dust over the Sahara and the link with the major atmospheric dynamical features over the region. We focus on the role of the WAM, cold pools, the Saharan heat low (SHL) and extra-tropical disturbances for enhancing dust emissions and modulating the 3D transport pathways of dust, over the dustiest region in the month of June 2011 (the latitude band from 17 to 23°N over the Sahara, e.g. Evan et al., 2015). The month of June is one of the dustiest periods over the central Sahara (e.g. over Tamanrasset in southern Algeria, Cuesta et al., 2008; Klose et al., 2010) and also the typical period of the onset of the WAM over the Sahel (see Fig. 1, e.g. Sultan and Janicot, 2000), triggering the formation of numerous dust-rising MCSs (e.g. Marsham et al., 2008). We choose to analyse this month for the year 2011 due to the availability of surface-based measurements from the Fennec intensive field campaign over the central Sahara (Washington et al., 2012), which are used as support for our study (sections 3.1 and 4.2).

First, we describe the AEROIASI approach (section 2.1), other datasets that are compared to it (sections 2.2 to 2.4) and the meteorological reanalysis used in the paper (section 2.5). Then, we present a validation of the capability of AEROIASI to retrieve the 3D distribution of dust over the Sahara, as compared with CALIOP in the vertical, MODIS, OMI and SEVIRI (Spinning Enhanced Visible and Infrared Imager) in the horizontal and AERONET (Aerosol Robotic Network, Holben et al., 1998) stations in absolute estimates of column integrated AOD (section 3). Afterwards, we detail a monthly analysis of the 3D distribution of dust over the Sahara and the associated dynamical features during June 2011 (section 4.1). Finally, we study the 3D distribution of dust when northward bursts of the WAM reach the central Sahara (section 4.2) and when it retreats south of this region (section 4.3), at daily scale as well as based on a composite view of several similar events. A summary is provided in section 5.

2. Datasets

2.1. AEROIASI over the Sahara

The AEROIASI algorithm is conceived to observe the 3D distribution of dust plumes for each overpass of IASI (Cuesta et al., 2015). These measurements offer global coverage twice daily at approximately 9h30 and 21h30 local time, with pixels spaced by 25 x 25 km^2 at nadir. The AEROIASI product is publicly available and can be provided on request. Here, we only use measurements of IASI on-board the MetOp-A satellite, which was the only MetOp satellite operational in June 2011. For the sake of better comparison with sun photometer data, we use here AEROIASI retrievals for morning overpasses of IASI (although AEROIASI data is available for all overpasses; see e.g. (Cuesta et al., 2015; Kylling et al., 2018)). The three-dimensional distribution of dust is obtained from vertical profiles of extinction coefficient at 10 µm derived for each IASI pixel under cloud-free conditions and over all surfaces, even for the bright surfaces of the Saharan desert and relatively low aerosol loads. A good agreement between dust extinction profiles derived from AEROIASI and the CALIOP lidar have been found, even for cases of moderate aerosol abundance (AOD ~ 0.15). AOD is directly derived from vertical integration and mean aerosol layer height is estimated as the height below which the AOD is half that of the total column. The retrieval is based on a constrained-least-squares fit with explicit radiative transfer calculations, where the vertical distribution and abundance of dust are iteratively adjusted in order to best fit IASI hyperspectral observations. Convergence is assured by auto-adaptive Tikhonov-Phillips-type constraints (Tikhonov, 1969) used for adjusting simultaneously the dust profile and surface temperature in order to offer good adaptability for different atmospheric and surface conditions. In order to limit the number of variables to be adjusted in the fitting procedure, surface emissivity is not modified during the retrievals. The information on the dust vertical distribution is provided by the spectral distribution of the measured infrared radiation over a relatively wide frequency range, which is mainly driven by thermal emission of the aerosol layers according to their temperatures and therefore their altitudes.

AEROIASI uses an *a priori* model of desert dust (including dust microphysical properties) and meteorological profiles provided as inputs to the line-by-line Karlsruhe Optimized and Precise Radiative transfer Algorithm (KOPRA) (Stiller et al., 2000). KOPRA is used to simulate thermal infrared radiance spectra and the inversion module KOPRAFIT to compare them to those measured by IASI, for 12 spectral micro-windows in the atmospheric window between 8 and 12 µm. KOPRA accounts for light absorption, emission and single scattering by aerosols, using dust optical properties derived at each wavelength with a Mie code. Multiple scattering by dust-particles are likely negligible in the thermal infrared (see more details in the work by Cuesta et al. (2015)). This is also the case for non-sphericity effects, except near the quartz resonant peak around 8.45 µm (Legrand et al., 2014). We expect that this effect is limited for AEROIASI, since this approach only uses IASI measurements from a single spectral

micro-window near 8.45 µm (accounting for only 3 % of the IASI channels used in the retrieval). The vertical grid is set between the surface and 12 km of altitude asl (above mean sea level), with 1 km increments. For each pixel, we use atmospheric temperature profiles and first guesses of surface temperatures and water vapor profiles from ECMWF reanalyses. In order to minimize the spectral residuals, the method adjusts iteratively the radiative transfer inputs (mainly the aerosol vertical profile and surface temperature) until convergence is reached (the maximum number of iterations is fixed to 10). The overall results of AEROIASI show that the degrees of freedom or the number of independent pieces of information (determined following Rodgers (2000)) in the retrieval of dust profiles varies during the iterative procedure, a typical value of ~1.5 being used to determine the shape of the dust extinction profiles. According to sensitivity analyses (Cuesta et al., 2015), AEROIASI retrievals are not very sensitive to the dust model parameters and the a priori profiles of dust and water vapour (below 5% for AOD and at most 14 % for the dust layer height), while the sensitivity is moderate with respect to the uncertainties of atmospheric and surface temperatures (typically below 15 %). Higher sensitivity (29 %) is only found for the retrieval of the AOD of elevated dust layers in the case of uncertainties of ± 2 K of a priori surface temperature.

The current paper uses AEROIASI retrievals from version 2 of the algorithm, which mainly differs from that described by Cuesta et al. (2015) in the *a priori* desert dust model and the surface emissivity database. The desert dust model consists of values of the spectral complex refractive indices, a single-mode lognormal particle size distribution and an *a priori* vertical profile. The spectral complex refractive indices are taken from the spectroscopic analysis of field samples of Saharan dust performed by Di Biagio et al. (2014). We use a modal radius (2.3 µm) and a modal width (standard deviation of 0.64) for the dust volume size distribution obtained by averaging volume effective radii and widths derived by AERONET measurements of the Zouerate station during June 2011 (from http://aeronet.gsfc.nasa.gov). This size distribution is consistent with the modal radius (~2.2 µm in terms of volume) of the medium-size mode of the size distribution measured by airborne in-situ sensors for major dust events during June 2011 and over central western Sahara in the framework of the FENNEC campaign (Ryder et al., 2013). Dust particles of this size range largely contribute to the total AOD in the thermal infrared and are transported over long distances. Fine dust particles (with radii < ~1 µm) account for less than 10% of the total AOD at 10 µm (e.g. Cuesta et al., 2015). In presence of freshly uplifted very large dust particles, AEROIASI retrievals may be moderately biased. We may expect a negative bias of less than 5 % in the AOD at 10 µm and a positive bias of less than 10 % for the mean dust layer height for an increase of the effective radii of dust by 10 % (Cuesta et al., 2015).

A first guess of the dust vertical distribution (the same profile for all pixels and all days) is considered in the inversion as background condition. This is obtained from an average of CALIOP extinction vertical profiles for dust over the Sahara during June 2011, scaled to particle concentration units in order to set an a priori AOD at 10 µm of 0.03.

The surface emissivity database is the same used in the inter-comparison of satellite retrievals of dust height performed by Kylling et al. (2018), derived from a global monthly IASI-derived climatology over land (Paul et al., 2012) and a surface temperature dependent model over ocean (Newman et al. 2005). Using these new databases, we obtain lower spectral residuals with respect to IASI measurements than with the previous version and higher adaptability for covering the tropical dust belt. Over this region, AEROIASI shows good performance for estimating the mean heights of dust layers (from the Atlantic to East Asia), corresponding to the lowest mean bias (−0.045 km) and RMSE (1.029 km) for a comparison with five other products (IASI and GOME-2-based methods) with respect to CALIOP-derived geometric mean dust heights (Kylling et al., 2018).

2.2. Aerosol optical depth from the AERONET ground-based network

In order to assess the quality of the AEROIASI dust observations over the Sahara, we perform comparisons like those shown by Cuesta et al. (2015) over East Asia. First, we compare AEROIASI retrievals of AOD with ground-based measurements from the AERONET sun photometer network. We consider 11 sites over the Sahara and the downwind Atlantic for the month of June 2011 (see the geographical location of the stations in Fig. 2e, note that level 1.5 data are used for considering all these stations). For consistency, the comparison is made between AOD from AEROIASI retrieved at 10 µm (mainly sensitivity to coarse particles) and extrapolated to 500 nm using an Angström exponent of 0.09 (derived from the climatological desert dust model, which accounts for absorptive differences in the spectral regions), and AERONET measurements of the so-called “coarse mode” AOD at 500 nm (available at http://aeronet.gsfc.nasa.gov, (O’Neill et al. 2003)). The criteria of spatio-temporal coincidence are ±30 min and ±1° of latitude and longitude (thus considering several measurements for each item of the comparison and avoiding too much heterogeneity). In order to ensure a comparison in cloud-free conditions and compare rather homogenous conditions, we only consider AERONET AOD observations with a temporal variability of less than 0.4 within ±1h. Furthermore, we impose a minimum of 3 pixels of quality checked AEROIASI retrievals and 2 AERONET measurements available per each item of the comparison. Then, we compare the average of all observations within the coincidence criteria, from AEROIASI and AERONET, for each site and each day of the comparison.

2.3. Aerosol horizontal distribution from SEVIRI, MODIS and OMI

For analysing the capability of AEROIASI to observe the horizontal distribution of Saharan dust, we compare it with other retrievals of dust AOD over the Sahara. We consider several satellite products based on different principles, two different methods from geostationary observations of SEVIRI in the thermal infrared (with 3-km spatial resolution and available only over land), i) one based on a physical approach from Imperial College London (ICL) (Brindley and Russell, 2009; and Banks and Brindley, 2013) here referred to "SEVIRI ICL" and ii) another based on a neural-network called here "SEVIRI NAS3" (North African Sand Storm Survey, Gonzalez and Briottet, 2017, http://nascube.univ-lille1.fr), iii) MODIS combined Dark-Target (Remer et al. 2005) and Deep-Blue (Hsu et al., 2004; Sayer et al., 2013) retrievals from measurements from the TERRA satellite (collection 6.1 product called MOD08_D3_v6.1) and iv) OMI data (product OMAERUVd_v003, Torres, 2008), these two last ones provided at 1 x 1° resolution by the GIOVANNI portal (https://giovanni.gsfc.nasa.gov/). In the figures, the colour scale for AEROIASI is different when compared to the other products (1.7 vs. 1). This accounts for the fact that AEROIASI is only sensitive to coarse particles (at 10 µm), whereas MODIS, OMI and AERONET retrieve total AOD at 500 nm and both SEVIRI products are scaled to visible total AOD for fine and coarse particle contributions. For temporal consistency with IASI measurements (around 0930 UTC for these days), we consider SEVIRI retrievals around 0930 UTC, MODIS retrievals from TERRA (around 1030 UTC) and AERONET measurements around 0930 UTC. OMI measurements are only available in the early afternoon (near 1330 UTC).

2.4. Aerosol vertical transects from CALIOP

We use vertical transects of aerosol extinction coefficient derived from CALIOP (Winker et al., 2007; 2009) over the Sahara to analyse the performance of AEROIASI to observe the vertical distribution of dust. In order to avoid unrealistically large particle extinction values near the surface, we derive dust extinction profiles from the inversion of CALIOP level 1 measurements (from http://www.icare.univ-lille1.fr) accounting for particle multiple scattering. This is recommended by the CALIOP Algorithm Theoretical Basis Document (Young et al., 2008) for dense dust layers, although this is not yet implemented in the official CALIOP level 2 products. As previously done over other regions e.g. (Cuesta et al., 2009, 2015), we use a classical inversion approach (Fernald et al., 1972; Fernald, 1984) considering a particle backscatter-to-extinction ratio of 0.024 sr^{-1} typical for dust (Cattral et al., 2005) modulated vertically by a multiple scattering coefficient (following Young et al. (2008)). As the time difference between CALIOP and IASI measurements is significant (at least 3-4 hours), we need to roughly match these two observations in order to compare the same air masses. For this, we sample AEROIASI data considering the horizontal drift of the air masses

observed by the CALIOP transect, estimated from wind fields from ERA5 reanalysis at the mean altitudes of the dust layers. Moreover, AEROIASI transects are obtained by averaging horizontally all available retrieved profiles within ±1° of latitude/longitude for the location of each CALIOP profile (a moving average). Before averaging, we interpolate AEROIASI profiles vertically every 100 m, in order to be able to depict finer resolution vertical features.

2.5. ERA5 meteorological reanalysis

Meteorological conditions leading to dust uplift and transport over the Sahara are described in section 4 using ERA5 reanalyses (Hersbach, 2016) produced by ECMWF (European Center for Medium-range Weather Forecast). We use meteorological fields (from http://climserv.ipsl.polytechnique.fr) with global coverage, a horizontal resolution of 0.25° x 0.25°, 137 levels and a time step of 1 hour. Wind, equivalent potential temperature, potential temperature and geopotential fields are used to describe transport patterns and the locations of the WAM, the SHL, extra-tropical disturbances and waves-like perturbations. We delineate the ITD as the location of the change in wind direction between south-westerly monsoon winds and north-easterly harmattan near the surface. For this, we combine two criteria usually used in previous research by detecting i) the change in meridional wind direction (e.g. Hastenrath, 1990; Sultan and Janicot, 2003), which is located north and in the vicinity of ii) the 15°C isodrosotherm (dew point) at 2 m (e.g. Lelé and Lamb, 2010). According to Flamant et al. (2009), when the ITD is reached by a cold pool formed within the monsoon area, the cold pool leading edge becomes locally the ITD. In that case, we replace the previous criteria for detecting the ITD by the location of the leading edge of the dust front uplifted by the cold pool (using AEROIASI for detecting the dust plume). We depict the southerlies and northerlies associated with wave-like perturbations from wind fields at 850 hPa filtered with a bandpass of 3–5 days (as usually done e.g. Cuesta et al., 2009; Lavaysse et al., 2010).

3. Validation of the AEROIASI approach over the Sahara

3.1. Dust optical depth

Figure 2 shows a good agreement of the AOD derived from AEROIASI and AERONET. Considering the total number of samples (147), the mean bias is low and positive (+0.02), the linear correlation R is high (0.90) and the room-mean-squared error (RMSE) between AODs is ~0.18 (Fig. 2a). For individual sites, correlations may increase, and mean biases typically range from -0.1 to +0.1 (see examples in Fig. 2b-d). The linear correlation for all stations over Northern Africa is higher than that found for East Asia (0.79), presumably linked to the fact that the contribution of aerosol species other than desert dust are

negligible over the Sahara during summertime. This correlation is similar to that from other IASI retrievals of dust AOD over Saharan AERONET stations over a longer time period (Capelle et al., 2018) and higher than that found over the tropical dust belt region (ranging from 0.45 to 0.8) by Popp et al., (2016).

The AOD time series for three stations at different latitudes and geographic settings (asterisks in Fig. 2e) shows the ability of AEROIASI to observe the daily evolution of the AOD for desert dust over the Sahara (Fig. 2b-d), both in the presence of dust events (timing and intensity, particularly for Tamanrasset and Dakar) and for background conditions of low dust load (see Saada station). Good AOD tracking ability by AEROIASI is also seen even for low AODs (e.g. at Saada, where a positive bias of about 0.1 is found). Two major dust events are well observed at Tamanrasset on 14 and 18 June 2011, in agreement with AERONET. Similar comparisons are found for other sites (not shown). The second AOD peak is associated with the major Saharan dust event investigated in detail in section 4.2.

Using these co-localized AERONET/AEROIASI datasets, we can also estimate a ratio of total AOD at 500 nm (sensitive to both fine and coarse particles) measured by sun photometers with respect to AEROIASI AOD retrievals at 10 µm (sensitive to coarse dust particles). This ratio, which is on average 1.7, is used in the next section (3.2) as scaling factor of the range of the colour bars for comparing AEROIASI AOD at 10 µm with other measurements of total AOD at 500 nm.

3.2. Dust horizontal distribution

We compare the horizontal distribution of AOD from AEROIASI with those from SEVIRI, MODIS and OMI for two typical major Saharan dust events, such as the one described in detail in section 4.2 (17 June). We also compare these satellite data with ground-based measurements of AOD from AERONET sites when available. Figures 3 and 4 highlight a particularly good consistency in the horizontal distribution of dust observed by AEROIASI and that from the two SEVIRI products, but also with AERONET AOD measurements when available. These three satellite products provide a coherent picture of a large dust plume of ~400 x 400 km^2 over the Central Sahara (centred at 18°N 2°E) on 17 June 2011 (Fig. 3a-c). It is transported north-westwards until covering an elongated area of ~1000 km the next day (centred at 22°N 2°E, Fig. 4a-c). For this large dust plume, AEROIASI and SEVIRI ICL retrieve similar AODs (respectively up to ~3.2 and ~3.0 on 17 June and ~2.5 and ~2.0 on 18 June) and SEVIRI NAS3 moderately higher values (~3.5 on 17 June and ~3.1 on 18 June). These values also agree reasonably with AERONET measurements (Fig. 3-4f) at Bordj Badji Mokhtar (21°N 1°E, AOD of ~4 on both days) but are significantly larger than at the mountain site

Tamanrasset on 17 June (23°N 5°E and 1320 m above sea level, total AOD of ~0.5) which might miss out dust in the lowest atmospheric layers.

The AEROIASI horizontal distribution of AOD is also fairly consistent with that shown by MODIS and OMI (Fig. 3-4d-e), but the latter ones present lower values of AOD over the Sahara than AEROIASI, SEVIRI and AERONET. The large dust plume over the Central Sahara is also depicted with high values of AOD by MODIS and OMI, but the MODIS AOD values are lower (~1) during both days and up to ~1 and ~2 for OMI respectively on 17 and 18 June. On 17 June, the horizontal shape of the dust plume observed with these instruments differs quite markedly from that of AEROIASI and SEVIRI. Greater consistency between the 5 satellite products is found with respect to the plume shape on 18 June.

Smaller dust plumes with high AOD (over ~1.5) are also retrieved by AEROIASI and the SEVIRI with a similar horizontal structure, e.g. north (25°N 2°E) and northwest (22°N 4°W) of the large dust plume over the central Sahara on 17 June (Fig. 3a-c). The MODIS dataset does not depict these two smaller dust plumes (with AOD~0.8) as clearly as the others satellite datasets. OMI shows high values of AOD (1.7) only near 20°N 4°W. All five satellite datasets show a dust plume southeast of the Sahara on 17 June (15°N 15°E) and southwest of the Sahara on 18 June (20°N 10°W). Only SEVIRI ICL shows dense dust plumes south of 15°N, which might be a spurious effect of unscreened clouds. Similar background values of AOD extending over most of the Sahara are retrieved by AEROIASI, SEVIRI ICL, MODIS and OMI, as well as AERONET data ranging from 0.3 to 0.5 (see complementary results comparing SEVIRI ICL, MODIS and AERONET by Banks et al. (2013)). The SEVIRI NAS3 dataset, however, shows lower background AOD values (~0.2).

In summary, these comparisons show an overall consistency of AEROIASI satellite observations of dust AOD with respect to other validated and widely used space-borne sensors (SEVIRI, MODIS and OMI) and ground-based observations (AERONET).

3.3. Dust vertical distribution

Comparisons between vertical transects of dust extinction coefficient from AEROIASI and CALIOP (respectively at 10 µm and 532 nm) are illustrated in Figure 5 for 2 cases on 17 and 19 June 2011 (no coincidences available on 18 June), respectively. These transects sample dense dust plumes during the dust outbreak over the Central Sahara analysed in detail in section 4.2. The overall vertical distributions depicted by these two datasets, AEROIASI and CALIOP, agree remarkably well. The same dust layers with similar vertical extents are found in both measurements. On 17 June, both active and passive observations show very clearly the same two dust plumes reaching the surface, at 15–17°N and 21–23°N, respectively, extending up to ~5 to 6 km and ~2.5 km of altitude and an elevated dust layer from ~3.5 to ~

5.5 km at 18–21°N. The near surface dust layers correspond to dust uplifted by strong winds along the leading edge of a cold cool (15–17°N, detected using SEVIRI AOD measurements) and enhanced harmattan winds (21–23°N), respectively. The elevated dust is located within a residual atmospheric boundary layer and corresponds to long-range transport from eastern sources (see more details in section 4). On 19 June, both datasets also agree in the depiction of a very dense dust layer extending from ~1 km to ~5 km of altitude at 20–22°N, resulting from dust uplifted by a cold pool and an elevated dust layer around 4 to 5 km of altitude reaching northward to 24.5°N. Some differences are also found, such as higher extinction values retrieved by AEROIASI for the dust layers at 15–17°N and an additional layer north of 25°N on 17 June. They could be linked to the temporal difference between the two datasets or uncertainties in the retrievals (e.g. cloud screening, the choice of backscatter-to-extinction ratio for CALIOP or dust and surface properties for AEROIASI). Overall, the agreement with CALIPSO observations illustrates the good capacity of AEROIASI to depict the vertical distribution of dust plumes and their horizontal extent along the CALIOP track.

4. Impact of WAM dynamical features on the 3D distribution of dust

In this section, we investigate the role of cold air intrusions associated with the WAM or deep convection-driven cold pools, as direct or indirect drivers of emissions and 3D transport of dust plumes over the central Sahara. This analysis is based on the new observations of AEROIASI of the 3D distribution of dust and ERA5 reanalysis data.

4.1. Daily evolution of dust over the central Sahara during June 2011

According to AEROIASI observations averaged over June 2011 (Fig. 6a), the largest values of AOD are clearly found over the point of the triple frontier of Algeria, Nigeria and Mali (i.e. the region 17–23°N 1–7°E). This area is a known large and systematic source of dust during summer (previously identified with SEVIRI data, Schepanski et al. 2007; Cuesta et al., 2008; Kocha et al., 2013). This hot spot is surrounded by the Aïr, Hoggar and Adrar des Ifoghas mountains respectively east, north and west of it (see Fig. 6c). According to 3D observations from AEROIASI (Fig. 6b), dust over this area extends vertically from the surface up to 5 km of altitude with highest abundance from 3 to 5 km and some localised maxima at the surface, probably linked to frequent dust emission. While the monthly average AOD at 10 µm for this region is higher than ~0.5, moderate values of about ~0.3 are observed across the whole of northern Africa in the latitude band from 13°N to 32°N. Over the Atlantic, dust is mainly transported in the latitude band from 10°N to 24°N as shown by higher AODs and winds

from the continent. On the contrary, north of 24°N the flow is from the Atlantic to the continent.

In the following, we focus on the dynamical features associated with the particularly high dust amounts over 17–23° 1–7°E, which is analysed in terms of the daily evolution of dust and meteorological variables presented as time/longitude Hovmöller graphs (Hovmöller, 1949) in Fig. 7–8 and time series centred over this region in Fig. 9. An original aspect of this Hovmöller analysis is that we distinguish between dust extinction at different altitudes for the first time, based on the new 3D observations of AEROIASI.

For the latitude band with maximum dust load (17–23°N), we observe different time/longitude evolutions of dust extinction depending on the altitude (Fig. 7c, f, i). At the surface, dust events mainly occur in two longitudes bands over the central (1°W–9°E) and western (18°–10°W) Sahara. High dust amounts do not show the slanted continuous pattern in time and longitude generally associated with transport. On the contrary, they are temporally distinct events, consistent with the behaviour of dust emissions. High surface dust loads are mostly observed in concomitance with high surface wind speeds (greater than approximately 5 m s^{-1}), in either the meridional, zonal or both directions. The two earliest peaks of surface dust (5 and 10 June) are concomitant with strong westerlies over the hot spot, probably associated with extra-tropical disturbances occurring northwest of Morocco (see the upper troughs in geopotential height anomalies at 300 hPa over 35–40°N in Fig. 8a). These disturbances are also seen above 2 km at 17–23°N as westerlies (strongest on 5 and 12 June, Fig. 7b, e) and southerlies moving westwards (at 1–7 °E on 5 June, Fig. 7a, d). The following four events of abundant surface dust (13–14, 17, 19–20 and 23 June) are triggered by the periodical occurrence of southerlies propagating westwards (along the green dashed lines in Fig. 7g). These surface winds are coherently preceded by easterlies and followed by westerlies (Fig. 7h), therefore suggesting cyclonic vortices (coincident with troughs of negative geopotential height anomalies - not shown). By manually tracking these four successive propagating features (also seen as southerlies at 2-3 km, Fig. 7d), we estimate a propagation speed c of 4–6 m s^{-1}, periods T of 3–5 days and wavelengths λ of 1500–2300 km. As they are first observed at the longitudes of the hot spot (1–7°E in the four cases), they are likely perturbations generated as a consequence of the convective activity over this area (see details at the end of this section). These wind structures have a wave-like behaviour, as they fulfil the wave relation (i.e. $c = \lambda / T$), have the same period as AEWs and also propagate along the AEJ (seen as easterlies above 2 km of altitude after 13 June, Fig. 7b, e). However, they are somewhat untypical. AEWs usually propagate faster (~8 m s^{-1}, e.g. Lafore et al., 2011), have longer wavelengths (2000–4000 km), are more intense at higher

altitudes (2–3 km or 850–700 hPa) and originate at a more eastern location (east of 20°E) than the waves observed over the hot spot from 13 to 23 June.

Elevated layers of high dust amounts are continuously observed over the central Sahara (1°W–9°E), without longitudinal transport until 13 June (both at 2–3 km and 4–5km of altitude, respectively in Fig. 7f, c). After this day, dust load above 2 km significantly increases and is advected westwards out to 20°W. Easterly transport is clearly linked to a change in zonal wind regime from westerlies at the beginning of the month (associated with extratropical disturbances northwest of Morocco) to sustained easterlies after 13 June, once the northern edge of the AEJ reaches this latitude band (see Fig. 7b, e). At 2–3 km of altitude, the highest dust loads are mainly observed over the Central Sahara (1°W – 9°E) and only some moderate dust amounts are transported westwards, whereas at 4–5 km the densest dust layers are observed during the period of transport from the central Sahara to the western Sahara (respectively in Fig. 7f, c).

Further details on the origin of the dust events over the central Sahara (17–23°N 1–7°E) during June 2011 are provided in Figures 8 and 9. Figure 9 shows time series of AOD derived from AEROIASI, an indicator of WAM northward excursions, the occurrence of haboobs associated with large MCSs (tracked with SEVIRI, as done in section 4.2) and ERA5 meridional winds at 850 hPa. The northward bursts of the WAM are depicted by the difference of equivalent potential temperature at 850 hPa between the location of the dust hotspot (17–23°N 1–7°E) and areas 8° east and 8° west from it (i.e. the longitudinal extent of a bulge of the ITD at this latitude being less than ~16°, e.g. Cuesta et al. 2009). A positive difference occurs for higher equivalent potential temperatures than the surrounding regions and is related to a regional northward advection of WAM air masses. The AOD time series clearly shows five periodical peaks every 3 or 4 days (on 10, 13, 17, 20 and 23 June). All these dust events are clearly concomitant with both cold pools initiated by MCSs and northward bursts of the WAM (which can also be pushed northward by cold pools). This means that in all cases dust is uplifted by both cold pools and/or the ITD acting as a density current. In addition to the northward transport of moist monsoonal air, one key factor favouring the convective activity that initiate the cold pools is probably the existence of mountains around the hot spot in central Sahara. Indeed, this is shown by the fact that haboobs in most of these cases form beneath MCSs located either over the Aïr (for the events of 10, 13, 17 and 20 June) or the Adrar des Ifoghas (on 19 June), as shown by SEVIRI observations (see the examples of 17 and 19 June in section 4.2). At this period of the year, orographic forcing appears to play an important role for convective initiation in this latitude band, as other favourable conditions (such as soil moisture) are expected to remain marginal.

Northward bursts of the WAM over the hot spot may also be favoured by synoptic conditions. This is the case for the cyclonic circulations associated with both extra-tropical disturbances located northwest of the Sahara at the beginning of the month (5 and 10 June, Fig. 8a) and the SHL after 16 June. Shortly before 16 June, the SHL moves from east of 0°E to northern Mauritania, reinforcing the northward burst of the WAM over the hot spot particularly on 16-17 June (shown by potential temperature anomaly at 850 hPa over 20–25°N in Fig. 8b). These large-scale transitions are typical for this period of the year (Knippertz et al., 2017). Moreover, northward bulges of the ITD are observed over the dust hot spot (17–23°N) on the 4 last dust events (after 13 June) and each of them propagates westwards from 7°E to 15°W in the following 2 or 3 days (see Hovmöller graph of equivalent potential temperature at 850 hPa, Fig. 8c). This occurs in clear concomitance with the propagation of the southerlies associated with the wave-like perturbations initiated over the hot spot (from the surface to 850 hPa, Fig. 7d, g). This means that the intense convective activity triggered near the dust hot spot not only affects this region, but also likely generates easterly propagating waves also favouring northward bursts of the WAM west from this region. This may contribute to enhance convection and associated dust emissions (see surface dust events concomitant the westward-propagating southerlies associated with these waves in Fig. 7i). Further investigation of the link dust/cold pools/WAM/waves in a 3D perspective is provided in the following section for the dustiest events of the month.

4.2. Dust outbreaks within northward bursts of the monsoon over the central Sahara

The largest dust outbreak over the central Sahara in June 2011 is initiated by a cold pool formed by a MCS over the Aïr mountains (18°N 7°E, see grey line in Fig. 10a) during the night from 16 to 17 June 2011, generating strong surface winds and the uplift of large amounts of dust (manually tracked with SEVIRI AOD images as shown in magenta in Fig. 10a). In the following hours, the dust plume becomes denser and extends over a larger region, with a leading edge moving north-westwards until reaching southern Algeria and eastern Mali during the morning of 17 June (see AEROIASI AOD at 1000 UTC in Fig. 10b). The north-western edge of the dust plume is located just south of the ITD, as the leading edge of MCS-generated cold pool has reached the ITD and merged with it at this time (as found by Flamant et al., 2009). This major dust plume is clearly co-located with the southerlies associated with a wave-like perturbation (probably generated by the convective activity that also forms the associated cold pool, Fig. 10g).

According to AEROIASI observations, the dust plume exhibits a leading edge heading north-westwards which extends from the surface up to 2–3 km of altitude (around 21°N 2°E, Fig. 10d-e) until 200–300 km behind it. Towards the rear south-eastern part of the plume, dust is only observed at 2-3 km of altitude and it does not reach the ground (seen over a ~200-km

wide band from 17°N 2°E to 21°N 4°E in Fig. 10d). A slanted shape is depicted by the mean altitudes of the dust plume increasing by 1–1.5 km from 21°N 2°E up to 20°N 3°E (Fig. 10c). At the surface, the variation of dust load clearly agrees with ground-based measurements of a nephelometer located at Bordj Badji Mokhtar (21.3°N 0.9°E) for this particular event (see Figure 5 of the paper by Allen et al., 2013). In situ measurements at the surface show a dust peak lasting for 5–6 hours, which is consistent with the passage of a 200–300 km wide dust front evidenced by AEROIASI propagating at ~12 m s^{-1} (estimated from SEVIRI by Allen et al., 2013).

A very similar 3D slanted structure of the dust plume over the hot spot (17–23°N 1–7°E) is also found for the two other major dust events occurring on 13 and 20 June 2011, in concomitance with cold pools and northward excursions of the WAM. A detailed description of the 3D structure of dust and the associated dynamical features is presented in Figure 11 as a 3D composite view of the 3 dustiest events (13, 17 and 20 June, highlighted by asterisks in Fig. 9). This composite can only be done with daily observations of the full 3D distribution of dust over the region, as provided by AEROIASI. Before averaging, we define a "0° normalized latitude and longitude" as the location on the leading edge of the dust front embedded within the strongest southerlies associated with the WAM burst. Then, we composite the 3D dust extinction, equivalent potential temperature and winds fields of the 3 events and represent them as transects (Fig. 11a, c) and graphs of iso-extinction and equivalent isentrope for the 3D distributions of dust and monsoonal air, respectively (Fig. 11d). This figure shows that the distribution of dust on the day of maximum AOD over the hot spot is consistently characterized by a dense dust front, extending from the surface up to ~2 km of altitude at the leading edge until about 2–3 degrees behind it (Fig. 11a, b). Behind this location (normalized latitude between -5 and -3° in Fig. 11a), the dust plume elevates up to 3.5 km of altitude and the near surface dust load is as low as in clean air, probably related to the monsoon flow. At the surface, dust loads are highest at the leading edge of the cold pool over a distance of 3 degrees (approximately 300 km, Fig. 11b) and decrease toward the rear of the plume, as found for the case of 17 June. The 3D picture (Fig. 11d) shows a rather rounded transversal shape of the dust front, where the leading edge is likely entrained westwards by the cyclonic circulation around the trough of the concomitant wave (see the dust plume front reaching the surface closer to the vortex).

The 3D slanted structure of the dust plume is consistent with the occurrence of dust uplift at the leading edge of the cold pool and subsequent transport of dust that elevates progressively following the slanted isentropes at the interface of the denser monsoon flow and the Saharan air layer (SAL) above (see Fig. 11a, c). A wind curl is seen behind/south of the leading edge of the dust front (Fig. 11a), which could be related to a perturbation of the

large-scale shallow circulation by the monsoon northward burst. A similar 3D slanted structure of the dust plume is also found up to 2 days after the AOD maxima within the area of southerlies behind the associated wave trough (after westward propagation of 3–4 degrees in longitude per day, see Fig. 12b, g). This is observed on 19 June when the dust plume initially uplifted over the central Sahara hot spot reaches north-western Mali and eastern Mauritania, still co-located with southerlies associated with a wave-like perturbation (see northern Mali in Fig. 12b, g). The dust of this plume has not only been emitted on 17 June but also on the evening of 18 June by an additional haboob formed by an MCS over the Adrar des Ifoghas mountains (grey lines in Fig. 12a). The northern part of the haboob is located just south of the ITD (reaching 23°N at these longitudes), extending from the ground up to 2–3 km over northern Mali (at 23°N 3°W in Fig. 12d) and dust is only seen at 2-3 km south of this region. The main differences with respect to the day of maximum AOD over the hot spot are a reduction of the dust amount by a factor of 2–3 and a less homogenous frontal structure of the dust plume.

Dust plumes with a slanted structure at the rear of the leading edge have been previously evidenced using airborne lidar observations (Bou Karam et al., 2007; Flamant et al., 2007; 2009), but only in 2D (along the aircraft track). AEROIASI shows here the first 3D observation of such dust frontal phenomena associated with the WAM, cold pool and wave activity.

4.3. Isentropic upgliding of dust during the retreat of the monsoon

During the period from 13 to 23 June, the central Sahara host spot (17–23°N 1–7°E) is reached by northerlies ahead of wave troughs approximately 2 days after large dust outbreaks are triggered over this area. We analyse the 3D distribution of dust during this situation at daily scale (on 19 June in Fig. 12) and from a composite of 3 similar cases occurring 2 days after the dust events over the hot spot (15, 19 and 22 June, in Fig. 13). Both points of view (on 19 June and the 3-case composite) show a contrasting situation when northerlies blow over the central Sahara hot spot with respect to that associated with southerlies, in terms of the 3D distribution of dust. In absence of a northward surge of the WAM, dust plumes reaching the surface are mainly observed north of the ITD, which is located at the southern edge of the hot spot (around 19°N, Fig. 12d). South of the ITD, elevated dust layers are seen at 2–5 km of altitude above monsoonal air (depicted by the 337 K isentrope iso-surface in Fig. 13d). Most of the dust layers located south of the ITD do not reach the ground. Contrary to the situation over the area of southerlies, these dust plumes are transported by isentropic upgliding with the residual SAL which is advected southwards above the monsoonal air.

5. Summary

This paper presents a new characterisation of the 3D distribution of dust and the link with the main WAM-related dynamic drivers over the central Sahara during June 2011, using hyperspectral satellite observations from IASI. This is the first analysis of daily observations of the full 3D distribution of dust over the Sahara, which are derived using the AEROIASI approach. Comparisons with independent datasets presented in this paper confirm a good performance of AEROIASI over the Sahara. For vertically integrated AOD of Saharan dust, AEROIASI shows a low mean bias (0.02), a good correlation (0.90) and a moderate mean squared difference (0.18) as compared with AERONET sun photometer measurements from 11 stations over the Sahara during June 2011. In a comparison of the horizontal distribution of AOD, AEROIASI show similar performance in relative terms on the location and structure of dust plumes with respect to other satellite observations (SEVIRI, MODIS, OMI) and a better quantitative match with two SEVIRI products (ICL and NAS3). Transects of vertical profiles of dust extinction across the Sahara are in very good agreement with CALIOP space-borne lidar data, in terms of vertical structure of dust layers along the track. This threefold validation using AODs as well as the horizontal and vertical distributions of dust gives confidence in AEROIASI observations for analysing the dynamical drivers of 3D distribution of Saharan dust.

According to a monthly average of AOD and 3D distribution of dust extinction from AEROIASI, we clearly identify the dustiest spot of the Sahara during June 2011 at the triple frontier of Algeria, Mali and Niger (17–23°N 1–7°E) over the Central Sahara. In this region, dust is distributed vertically from the surface up to 5 km of altitude, with highest monthly dust loads from 3 to 5 km of altitude. A daily time series of AOD over this area reveals a periodical evolution of dust abundance, with 5 major peaks during the month occurring every 3–4 days. Our study shows that all these dust load peaks are indeed concomitant in time and space with northward excursions of the WAM and cold pools generated by convective activity. Convective initiation is enhanced by the presence of the Aïr and Adrar des Ifoghas mountains east and west of the hot spot.

Two clearly distinct regimes in terms of atmospheric conditions over northern Africa are observed before and after 13 June 2011 (see schematics in Fig. 14). At the beginning of the month, extra-tropical disturbances located northwest of Morocco significantly affect atmospheric circulation as far as the central Sahara. The cyclonic circulation associated to these troughs favours the occurrence of northward bursts of the WAM and the associated southerly advection of moist air over the hot spot. This occurs during 2 dust outbreaks over this region, a moderate event on 5 June and a major one on 10 June. These dust plumes are not remotely transported, as zonal winds are perturbed by the extra-tropical troughs and the AEJ is still located south of the hot spot.

After 13 June, no more major extra-tropical disturbances are seen to directly affect the ITD region and the AEJ moves north until reaching the hot spot. During this period and in the latitude band 17–23°N, elevated dust layers between 2 and 5 km are visibly transported westward by the AEJ (from the longitude band 0–10°E to 20–10°W). Over the hot spot, intense convection activity forms a succession of 4 haboobs every 3 or 4 days (on 13, 17, 20 and 23 June) and also generate wave-like perturbations that propagate westwards along the AEJ. These waves have periods of 3–5 days as those of typical AEWs, but they differ from these with respect to other properties (altitude of maximum intensity, propagation speed, wavelength). Both phenomena, haboobs and waves, contribute to the occurrence of concomitant northward bulges of the ITD over the hot spot, which then propagate westwards in concomitance with the southerlies behind the trough of the wave-like perturbations in the following 2 or 3 days. Shortly before 16 June, the SHL moves westward until reaching northern Mauritania and intensifies. After 16 June, the cyclonic circulation associated with the SHL adds as a third factor favouring the northward surge of the WAM over the hot spot.

Additional insights on how dynamical drivers affect the 3D distribution of dust are obtained from the analysis of (a) the dustiest event of the month between 17 and 19 June 2011 and (b) a composite of the 3 dustiest events coincident with northward excursions of the WAM (on 13, 17 and 20 June). On the day of maximum AOD over the hotspot at the triple frontier of Algeria, Niger and Mali an elongated dust front is transported northwards by the southerlies associated with the convective activity over the area. The leading edge of the dust plume extends from the surface up to 2 km of altitude and its tail progressively elevates up to 3.5 km until 500 km behind the leading front. Around 200 km behind the front dust, surface concentrations drop, and a slanted layer of dust elevates over clean air beneath (probably brought in by the monsoon flow behind the frontal structure). Haboobs formed the night before also play a role as an efficient mechanism for dust uplift and contribute to the formation of the dust front. Once uplifted, these dust plumes are advected north-westwards by the cyclonic vortex circulation at the trough of a wave-like perturbation generated by convection over the hot spot, still forming a leading edge extending from the surface to about 2 km of altitude, but less abundant in terms of dust load and a less sharp frontal structure. A contrasting situation is found in absence of northward bursts of the WAM, where most dust is observed at elevated atmospheric layers around 3–5 km and thus where the SAL is transported slantwise southwards following the ascending isentropes above the WAM layer.

These results show new observational evidence of the importance of the WAM, cold pools, extra-tropical disturbances and the SHL as drivers of the 3D distribution of dust over the

Central Sahara during summer. Future studies of the 3D distribution of dust based on AEROIASI data will enable a quantitative estimation of the role of these mechanisms in the emission and transport of Saharan dust at the climatological scale. These analyses will provide valuable information on dust vertical mixing processes, which are difficult to model, and play a crucial role on the diurnal cycle. New insight of dust emission occurrence and location may be provided by AEROIASI in combination with back-trajectories, given its capability to depict dust variability near the surface with less ambiguities than standard vertically integrated satellite measurements. AEROIASI will also be used for validating model simulations of the horizontal and vertical distribution of dust, with the latter being currently very rarely validated. In addition, AEROIASI observations provide a new and unique three-dimensional constraint for models via data assimilation, as current state-of-the-art systems only assimilate the horizontal distribution of AOD, typically provided by MODIS (e.g. Bozzo et al., 2019).

Acknowledgements

The authors are grateful for the financial support given by the Centre National des Etudes Spatiales (CNES, the French Space Agency, IASI project/Terre, Océan, Surfaces continentals, Atmosphère), the Programme National de Télédétection Spatiale (PNTS, http://programmes.insu.cnrs.fr/pnts, grant n° PNTS-2013-05, project "SYNAEROZON") and the Agence Nationale de la Recherche (ANR grant 2010 BLAN 606 01) for achieving this research work and its publication. This study is also supported by the Université Paris Est Créteil (UPEC) and the Centre National des Recherches Scientifiques – Institut National des Sciences de l'Univers (CNRS-INSU). We thank the Institut für Meteorologie und Klimaforschung of the Karlsruhe Institute of Technology (Germany) for providing the KOPRA radiative transfer code for processing IASI data. IASI is a joint mission of EUMETSAT and CNES. We acknowledge Jamie Banks from Imperial College London (United Kingdom) and Louis Gonzalez from the Laboratoire d'Optique Atmosphérique (France) for providing their SEVIRI aerosol products (respectively called here SEVIRI ICL and SEVIRI NAS3, http://nascube.univ-lille1.fr), the AERONET network for sun photometer observations over the Sahara (http://aeronet.gsfc.nasa.gov), the data centers AERIS (https://www.aeris-data.fr) for the level 1 data of IASI (originally supplied by EUMETSAT, http://www.eumetsat.int) and the GIOVANNI portal (https://giovanni.gsfc.nasa.gov) for MODIS and OMI level 3 datasets. Meteorological reanalyzes produced by ECMWF and CALIOP measurements (originally from NASA, http://ladsweb.nascom.nasa.gov) are supplied by CLIMSERV (http://climserv.ipsl.polytechnique.fr). Moreover, we would like to thank Richard Washington from Keble College (Oxford, UK), John Marsham from the University of Leeds (Leeds, UK) and Claire Ryder from the University of Reading (Reading, UK) for kindly providing some ancillary data (useful for discussions, although not directly used in the paper).

References

Banks, J. R. and H. E. Brindley, H. E. 2013. Evaluation of MSG-SEVIRI mineral dust retrieval products over North Africa and the Middle East. Remote Sens. Environ., 128, 58-73.

Banks, J. R., H. E. Brindley, C. Flamant, M. J. Garay, N. C. Hsu, O. V. Kalashnikova, L. Klüser, and A. M. Sayer. 2013. Intercomparison of satellite dust retrieval products over the west African Sahara during the Fennec campaign in June 2011, Remote Sens. Environ., 136, 99-116.

Bangert, M., Nenes, A., Vogel, B., Vogel, H., Barahona, D., Karydis, V. A., Kumar, P., Kottmeier, C., and Blahak, U. 2012. Saharan dust event impacts on cloud formation and radiation over Western Europe. Atmos. Chem. Phys., 12, 4045–4063, https://doi.org/10.5194/acp-12-4045-2012.

Berthier, S., P. Chazette, P. Couvert, J. Pelon, F. Dulac, F. Thieuleux, C. Moulin, and T. Pain. 2006. Desert dust aerosol columnar properties over ocean and continental Africa from Lidar in-Space Technology Experiment (LITE) and Meteosat synergy, J. Geophys. Res.,111, D21202, doi:10.1029/2005JD006999.

Bock O, Bouin MN, Doerflinger E, Collard P, Masson F, Meynadier R, Nahmani S, Koite M, Gaptia Lawan Balawan K, Dide F, Ouedraogo D, Pokperlaar S, Ngamini J-B, Lafore J-P, Janicot S, Guichard F, Nuret M. 2008. West African Monsoon observed with ground-based GPS receivers during African Monsoon Multidisciplinary Analysis (AMMA). J. Geophys. Res. 113: D21105, DOI:10.1029/2008JD010327.

Bou Karam, D., C. Flamant, P. Knippertz, O. Reitebuch, J. Pelon, M. Chong, and A. Dabas. 2008. Dust emissions over the Sahel associated with the West African monsoon inter-tropical discontinuity region: A representative case study, Q. J. R. Meteorol. Soc., 134, 621–634.

Bozzo, A., Benedetti, A., Flemming, J., Kipling, Z., and Rémy, S. 2019. An aerosol climatology for global models based on the tropospheric aerosol scheme in the Integrated Forecasting System of ECMWF, Geosci. Model Dev. Discuss., https://doi.org/10.5194/gmd-2019-149, in review.

Brindley, H. E. and J. E. Russell. 2009. An assessment of Saharan dust loading and the corresponding cloud - free longwave direct radiative effect from geostationary satellite observations. J. Geophys. Res., 114(D23).

Callewaert, S., Vandenbussche, S., Kumps, N., Kylling, A., Shang, X., Komppula, M., Goloub, P., and De Mazière, M. 2019. The Mineral Aerosol Profiling from Infrared Radiances (MAPIR)

algorithm: version 4.1 description and evaluation, Atmos. Meas. Tech., 12, 3673–3698, https://doi.org/10.5194/amt-12-3673-2019.

Capelle, V., Chédin, A., Pondrom, M., Crevoisier, C., Armante, R., Crepeau, L., Scott, N. A. 2018. Infrared dust aerosol optical depth retrieved daily from IASI and comparison with AERONET over the period 2007–2016. Rem. Sens. Env., 206, 15-32.

Cattrall C, J. Reagan, K. Thome, O. Dubovik. 2005. Variability of aerosol and spectral lidar and backscatter and extinction ratios of key aerosol types derived from selected Aerosol Robotic Network locations, J. Geophys Res., 110 (D10S11), DOI:10.1029/2004JD005124.

Chaboureau, J. P., Flamant, C., Dauhut, T., Kocha, C., Lafore, J. P., Lavaysse, C., Marnas F., Mokhatari M., Pelon J., Reinares Martinez I., Schepanski, K., P. Tulet, 2016. Fennec dust forecast intercomparison over the Sahara in June 2011. Atmos. Chem. Phys. 16, 6977–6995, https://doi.org/10.5194/acp-16-6977-2016.

Couvreux F, Guichard F, Bock O, Lafore J-P, Redelsperger JL. 2009. Monsoon flux pulsations over West Africa prior to the monsoon onset. Submitted to Q. J. R. Meteorol. Soc. 135: AMMA special edition.

Cuesta J, Edouart D, Mimouni M, Flamant PH, Loth C, Gibert F, Marnas F, Bouklila A, Kharef M, Ouchène B, Kadi M, Flamant C. 2008. Multiplatform observations of the seasonal evolution of the Saharan atmospheric boundary layer in Tamanrasset, Algeria, in the framework of the African Monsoon Multidisciplinary Analysis field campaign conducted in 2006. J. Geophys. Res. 113: D00C07, DOI:10.1029/2007JD009417.

Cuesta, J., J. Marsham, D. Parker and C. Flamant. 2009. Dynamical mechanisms controlling the vertical redistribution of dust and the thermodynamic structure of the West Saharan Atmospheric Boundary Layer during Summer, Atmos. Sci. Lett., doi: 10.1002/asl.207.

Cuesta, J., Lavaysse, C., Flamant, C., Mimouni, M., Knippertz, P. 2010. Northward bursts of the West African monsoon leading to rainfall over the Hoggar Massif, Algeria. Q. J. R. Meteorol. Soc., 136(S1), 174-189.

Cuesta, J., M. Eremenko, C. Flamant, G. Dufour, B. Laurent, G. Bergametti, M. Hopfner, J. Orphal and D. Zhou. 2015. Three-dimensional distribution of a major desert dust outbreak over East Asia in March 2008 derived from IASI satellite observations. J. Geophys. Res. 120: 7099-7127.

DeSouza-Machado, S. G., L. L. Strow, B. Imbiriba, K. McCann, R. M. Hoff, S. E. Hannon, J. V. Martins, D. Tanré, J. L. Deuzé, F. Ducos and O. Torres. 2010. Infrared retrievals of dust using AIRS: Comparisons of optical depths and heights derived for a North African dust storm to other collocated EOS A-Train and surface observations, J. Geophys. Res., 115, D15.

Di Biagio, C., H. Boucher, S. Caquineau, S. Chevaillier, J. Cuesta, and P. Formenti. 2014. Variability of the infrared complex refractive index of African mineral dust: experimental estimation and implications for radiative transfer and satellite remote sensing, Atmos. Chem. Phys., 14, 11093–11116.

Dunion, J. P. and C. S. Velden. 2004. The impact of the Saharan air layer on Atlantic tropical cyclone activity, Bull. Am. Meteorol. Soc., 85 (3), 353-365.

Evan, A. T., Flamant, C., Lavaysse, C., Kocha, C., & Saci, A. 2015. Water vapor–forced greenhouse warming over the Sahara Desert and the recent recovery from the Sahelian drought. Journal of Climate, 28(1), 108-123.

Fernald, F.G., B.M. Herman and J.A. Reagan. 1972. Determination of aerosol height distributions by lidar, J. Appl. Meteorol., 11, 482-489.

Fernald, F.G. 1984. Analysis of atmospheric lidar observations - Some comments, Appl. Optics, 23 (5), 652-653.

Fink AH, Reiner A. 2003. Spatiotemporal variability of the relation between African Easterly Waves and West African squall lines in 1998 and 1999. J. Geophys. Res. 108: 4332,DOI:10.1029/2002JD002816.

Flamant C, Chaboureau J-P, Parker DJ, Taylor CM, Cammas J-P, Bock O, Timouk F, Pelon J. 2007. Airborne observations of the impact of a convective system on the planetary boundary layer thermodynamics and aerosol distribution in the inter-tropical discontinuity region of the West African Monsoon. Q. J. R. Meteorol. Soc. 133: 1175–1189.

Flamant C, Knippertz P, Parker DJ, Chaboureau J-P, Lavaysse C, Agusti-Panareda A, Kergoat L. 2009. The impact of a mesoscale convective system cold pool on the northward propagation of the intertropical discontinuity over West Africa. Q. J. R. Meteorol. Soc. 135: 139–159.

Francis, D., Alshamsi, N., Cuesta, J., Gokcen Isik, A., & Dundar, C. 2019. Cyclogenesis and density currents in the Middle East and the associated dust activity in September 2015. Geosciences, 9(9), 376.

Gonzalez, L., and Briottet, X. 2017. North Africa and Saudi Arabia day/night sandstorm survey (NASCube). Remote Sensing, 9(9), 896.

Guichard, F., Kergoat, L., Mougin, E., Timouk, F., Baup, F., Hiernaux, P., & Lavenu, F. 2009. Surface thermodynamics and radiative budget in the Sahelian Gourma: Seasonal and diurnal cycles. J. Hydrol., 375(1-2), 161-177.

Guo, J., H. Xu, L. Liu, D. Chen, Y. Peng, S. H. L. Yim, Y. Y. J. Li, C. Zhao and P. Zhai. 2019. The Trend Reversal of Dust Aerosol Over East Asia and the North Pacific Ocean Attributed to

Large - Scale Meteorology, Deposition, and Soil Moisture. J. Geophys. Res.: Atmos., 124(19), 10450-10466, doi:10.1029/2019JD030654.

Hastenrath, S. 1990. Decadal-scale changes of the circulation in the tropical Atlantic sector associated with Sahel drought. Int. J. Climatol.,10, 459–472.

Haywood, J. and Boucher, O. 2000. Estimates of the direct and indirect radiative forcing due to tropospheric aerosols: A review. Rev. Geophys., 38(4), 513-543.

Heald, C. L., Ridley, D. A., Kroll, J. H., Barrett, S. R. H., Cady-Pereira, K. E., Alvarado, M. J., & Holmes, C. D. 2014. Contrasting the direct radiative effect and direct radiative forcing of aerosols. Atmos. Chem. Phys., 14(11), 5513-5527.

Hersbach, H. 2016. The ERA5 Atmospheric Reanalysis. In AGU Fall Meeting Abstracts. Abstract #NG33D-01.

Holben, B. N., T. F. Eck, I. Slutsker, D. Tanre, J. P. Buis, A. Setzer, E. Vermote, J.A. Reagan, Y.J. Kaufman, T. Nakajima, F. Lavenu, I. Jankowiak and A. Smirnov. 1998. AERONET-A federated instrument network and data archive for aerosol characterization, Remote Sens. Environ., 66 (1), 1-16.

Hovmöller, E. 1949. The trough-and-ridge diagram. Tellus, 1(2), 62-66.

Hsu, N. C., S.C. Tsay, M. D. King and J. R. Herman. 2004. Aerosol properties over bright-reflecting source regions. IEEE Trans. Geosci. Rem. Sens., 42(3), 557-569.

Jones, C., N. Mahowald, C. Luo. 2004. Observational evidence of African desert dust intensification of easterly waves, Geophys. Res. Lett., 31 (17).

Klose, M., Shao, Y., Karremann, M. K., and Fink, A. H. 2010. Sahel dust zone and synoptic background. Geophys. Res. Lett., 37(9).

Knippertz, P., Deutscher, C., Kandler, K., Müller, T., Schulz, O., Schütz, L. 2007. Dust mobilization due to density currents in the Atlas region: Observations from the Saharan Mineral Dust Experiment 2006 field campaign. J. Geophys. Res., 112(D21).

Knippertz, P. 2008. Dust emissions in the West African heat trough–the role of the diurnal cycle and of extratropical disturbances. Meteorol. Z., 17(5), 553-563.

Knippertz, P. and Todd, M. C. 2010. The central west Saharan dust hot spot and its relation to African easterly waves and extratropical disturbances. J. Geophys. Res., 115(D12).

Knippertz, P., Stuut, J. B. W. 2014. Mineral dust. Springer Dordrecht Heidelberg New York London, https://doi.org/10.1007/978-94-017-8978-3, 10, 978-94.

Knippertz, P., Fink, A. H., Deroubaix, A., Morris, E., Tocquer, F., Evans, M. J., Flamant, C., Gaetani, M., Lavaysse, C., Mari, C., Marsham, J. H., Meynadier, R., Affo-Dogo, A., Bahaga, T., Brosse, F., Deetz, K., Guebsi, R., Latifou, I., Maranan, M., Rosenberg, P. D., and Schlueter, A. 2017. A meteorological and chemical overview of the DACCIWA field campaign in West Africa in June–July 2016, Atmos. Chem. Phys., 17, 10893–10918, https://doi.org/10.5194/acp-17-10893-2017.

Kocha, C., Tulet, P., Lafore, J. P., Flamant, C. 2013. The importance of the diurnal cycle of Aerosol Optical Depth in West Africa. Geophys. Res. Lett., 40(4), 785-790.

Kylling, A., Vandenbussche, S., Capelle, V., Cuesta, J., Klüser, L., Lelli, L., Popp, T., Stebel, K., and Veefkind, P. 2018. Comparison of dust-layer heights from active and passive satellite sensors, Atmos. Meas. Tech., 11, 2911–2936, https://doi.org/10.5194/amt-11-2911-2018.

Lafore, J.-P., Flamant, C., Guichard, F., Parker, D. J., Bouniol, D., Fink, A. H., Giraud, V., Gosset, M., Hall, N., Holler, H., Jones, S. C., Protat, A., Roca, R., Roux, F., Said, F., and Thorncroft, C. 2011. Progress in understanding of weather systems in West Africa, Atmos. Sci. Lett., 12, 7–12, doi:10.1002/asl.335.

Lavaysse, C., Flamant, C., Janicot, S., Knippertz, P. 2010. Links between African easterly waves, midlatitude circulation and intraseasonal pulsations of the West African heat low. Q. J. R. Meteorol. Soc., 136(S1), 141-158.

Legrand, M., O. Dubovik, T. Lapyonok, and Y. Derimian. 2014. Accounting for particle non-sphericity in modeling of mineral dust radiative properties in the thermal infrared, J. Quant. Spectrosc. Radiat. Transfer, 149, 219–240.

Lélé, I. M., and Lamb, P. J. 2010. Variability of the intertropical front (ITF) and rainfall over the West African Sudan–Sahel zone. J. Climate, 23(14), 3984-4004.

Liu, L., J. Guo, H. Gong, Z. Li, W. Chen, R. Wu, R., L. Wang, H. Xu, J. Li, D. Chen and P. Zhai. (2019). Contrasting influence of Gobi and Taklimakan deserts on the dust aerosols in western North America. Geophys. Res. Lett., 46(15), 9064-9071, doi: 10.1029/2019GL083508.

Lothon, M., Saïd, F., Lohou, F., Campistron, B. 2008. Observation of the diurnal cycle in the low troposphere of West Africa. Mon. Wea. Rev., 136(9), 3477-3500.

Mahowald, N. M., S. Kloster, S. Engelstaedter, J. Keith Moore, S. Mukhopadhyay, Joseph R. McConnell, S. Albani, S. C. Doney, A. Bhattacharya, M. A. J. Curran, M. G. Flanner, F. M. Hoffman, D. M. Lawrence, K. Lindsay, P. A. Mayewski, J. Neff, D. Rothenberg, E. Thomas, P. E. Thornton, C. S. Zender. 2001. Observed 20th century desert dust variability: impact on climate and biogeochemistry, Atmos. Chem. Phys., 10 (22), 10875-10893.

Mahowald, N., A. Baker, G. Bergametti, N. Brooks, R. Duce, T. Jickells, N. Kubilay, J. Prospero, I. Tegen. 2005. Atmospheric global dust cycle and iron inputs to the ocean, Global Biogeochem. Cycles, 19(4), GB4025,10.1029/2004GB002402.

Mahowald, N., J.-A. Ballentine, J. Feddema, N. Ramankutty. 2007. Global trends in visibility: implications for dust sources, Atmos. Chem. Phys., 7, 3309-3337.

Marsham JH, Parker DJ, Grams CM, Taylor CM, Haywood JM. 2008. Uplift of Saharan dust south of the intertropical discontinuity. J. Geophys. Res. 113: D21102, DOI:10.1029/2008JD009844.

Meloni, D., Di Sarra, A., Di Iorio, T., Fiocco, G. 2005. Influence of the vertical profile of Saharan dust on the visible direct radiative forcing. J. Quant. Spectr. Radiat. Trans., 93(4), 397-413.

Newman, S. M., Smith, J. A., Glew, M. D., Rogers, S. M., Taylor, J. P. 2005. Temperature and salinity dependence of sea surface emissivity in the thermal infrared. Q. J. R. Meteorol. Soc. 131(610), 2539-2557.

O'Neill, N. T., T. F. Eck, A. Smirnov, B. N. Holben, and S. Thulasiraman. 2003. Spectral discrimination of coarse and fine mode optical depth, J. Geophys. Res., 108 (D17).

Paul, M., Aires, F., Prigent, C., Trigo, I. F., Bernardo, F. 2012. An innovative physical scheme to retrieve simultaneously surface temperature and emissivities using high spectral infrared observations from IASI. J. Geophys. Res. 117(D11).

Prospero, J. M. 1999. Assessing the impact of advected African dust on air quality and health in the eastern United States. Human Ecol. Risk Assess., 5(3), 471-479.

Remer, L. A., Y. J. Kaufman, D. Tanré, S. Mattoo, D. A. Chu, J. Vanderlei Martins, R-R. Li, C. Ichoku, R. C. Levy, R. G. Kleidman, T. F. Eck, E. Vermote and B. N. Holben. 2005. The MODIS aerosol algorithm, products, and validation, J. Atmos. Sci., 62 (4), 947-973.

Sayer, A. M., N. C. Hsu, C. Bettenhausen, and M-J. Jeong. 2013. Validation and uncertainty estimates for MODIS Collection 6 Deep Blue aerosol data, J. Geophys. Res., 14, 7864-7872.

Pierangelo, C., Chédin, A., & Chazette, P. 2004. Measurements of stratospheric volcanic aerosol optical depth from NOAA TIROS Observational Vertical Sounder (TOVS) observations. J. Geophys. Res., 109(D3).

Popp, T., de Leeuw, G., Bingen, C., Brühl, C., et al. 2016. Development, Production and Evaluation of Aerosol Climate Data Records from European Satellite Observations (Aerosol_cci), Rem. Sens., 8, 1–34, https://doi.org/10.3390/rs8050421.

Rodgers, C. D. 2000. Inverse methods for atmospheric sounding: Theory and practice, World Scientific Publishing Company, London, UK.

Roberts, A. and Knippertz, P. 2012. Haboobs: convectively generated dust storms in West Africa. Weather, 67(12), 311-316.

Roberts, A. J. and Knippertz, P. 2014. The formation of a large summertime Saharan dust plume: Convective and synoptic-scale analysis. J. Geophys. Res., 119(4), 1766-1785.

Ryder, C. L., Highwood, E. J., Rosenberg, P. D., Trembath, J., Brooke, J. K., Bart, M., Dean, A., Crosier, J., Dorsey, J., Brindley, H., Banks, J., Marsham, J. H., McQuaid, J. B., Sodemann, H., and Washington, R. 2013. Optical properties of Saharan dust aerosol and contribution from the coarse mode as measured during the Fennec 2011 aircraft campaign, Atmos. Chem. Phys., 13, 303–325, https://doi.org/10.5194/acp-13-303-2013.

Schepanski, K., Tegen, I., Laurent, B., Heinold, B. and Macke, A. 2007. A new Saharan dust source activation frequency map derived from MSG-SEVIRI IR-channels. Geophys. Res. Lett., 34(18).

Stiller, G. P. (Ed.) with contributions from T. v. Clarmann, A. Dudhia, G. Echle, B. Funke, N. Glatthor, F. Hase, M. Höpfner, S. Kellmann, H. Kemnitzer, M. Kuntz, A. Linden, M. Linder, G.P. Stiller and S. Zorn. 2000. The Karlsruhe Optimized and Precise Radiative Transfer Algorithm (KOPRA), vol. FZKA 6487 of Wissenschaftliche Berichte, Forschungszentrum Karlsruhe, Germany.

Su, X., P. Goloub, I. Chiapello, H. Chen, F. Ducos and Z. Li. 2010. Aerosol variability over East Asia as seen by POLDER space-borne sensors. J. Geophys. Res.,115 (D24).

Sultan B, Janicot S. 2000. Abrupt shift of the ITCZ over West Africa and intra-seasonal variability. Geophys. Res. Lett. 27: 3353–3356.

Sultan B. Janicot S. 2003. The West African monsoon dynamics. Part II: The ‘preonset’ and ‘onset’ of the summer monsoon. J. Climate 16: 3407–3427.

Tikhonov, A. 1963. On the solution of incorrectly stated problems and a method of regularization, Dokl. Acad. Nauk SSSR, 151, 501–504.

Torres, O., A. Tanskanen, B. Veihelmann, C. Ahn, R. Braak, P. K. Bhartia, P. Veefkind and P. Levelt. 2007. Aerosols and surface UV products from Ozone Monitoring Instrument observations: An overview. J. Geophys. Res., 112 (D24).

Vandenbussche, S., S. Kochenova, A. C. Vandaele, N. Kumps and M. De Mazière. 2013. Retrieval of desert dust aerosol vertical profiles from IASI measurements in the TIR atmospheric window, Atmos. Meas. Tech., 6, 2577–2591, doi:10.5194/amt-6-2577-2013.

Washington, R. and Todd, M. C. 2005. Atmospheric controls on mineral dust emission from the Bodélé Depression, Chad: The role of the low level jet. Geophys. Res. Lett., 32(17).

Washington, R., Flamant, C., Parker, D. J., Marsham, J., McQuaid, J. B., Brindley, H., Todd, M., Highwood, E. J., Chaboureau, J.-P., Kocha, C., Bechir, M., Saci, A., and Ryder, C. L. 2012. Fennec – The Saharan Climate System, CLIVAR Exchanges, No. 60, International CLIVAR Project Office, Southampton, United Kingdom, 31–32.

Xu, X., J. Gao, J. Gao and Y. Chen. 1994. Air pollution and daily mortality in residential areas of Beijing, China. Arch. Environ. Health, 49 (4), 216-222.

Yoshioka M., N. Mahowald, A. Conley, W. Collins, D. Fillmore, C. Zender, D. Coleman. 2007. Impact of Desert Dust Radiative Forcing on Sahel Precipitation: Relative importance of dust compared to sea surface temperature variations, vegetation changes and greenhouse gas warming, J. Clim., 20,1445-1467, DOI:10.1175/JCLI4056.1.

Young S, Winker D, Vaughan M, Hu Y, Kuehn R. 2008. Extinction Retrieval Algorithms, CALIOP algorithm theoretical basis document PC-SCI-202 Part 4, Available on http://www-calipso.larc.nasa.gov/ resources/pdfs/PC-SCI-202 Part4 v1.0.pdf.

Yu, H., L. A. Remer, M. Chin, H. Bian, Q. Tan, T. Yuan and Y. Zhang. 2012. Aerosols from overseas rival domestic emissions over North America. Science, 337(6094), 566-569, doi: 10.1126/science.1217576.

Winker DM, Hunt WH, McGill MJ. 2007. Initial performance assessment of CALIOP. Geophys. Res. Lett. 34: L19803, DOI:10.1029/2007GL030135.

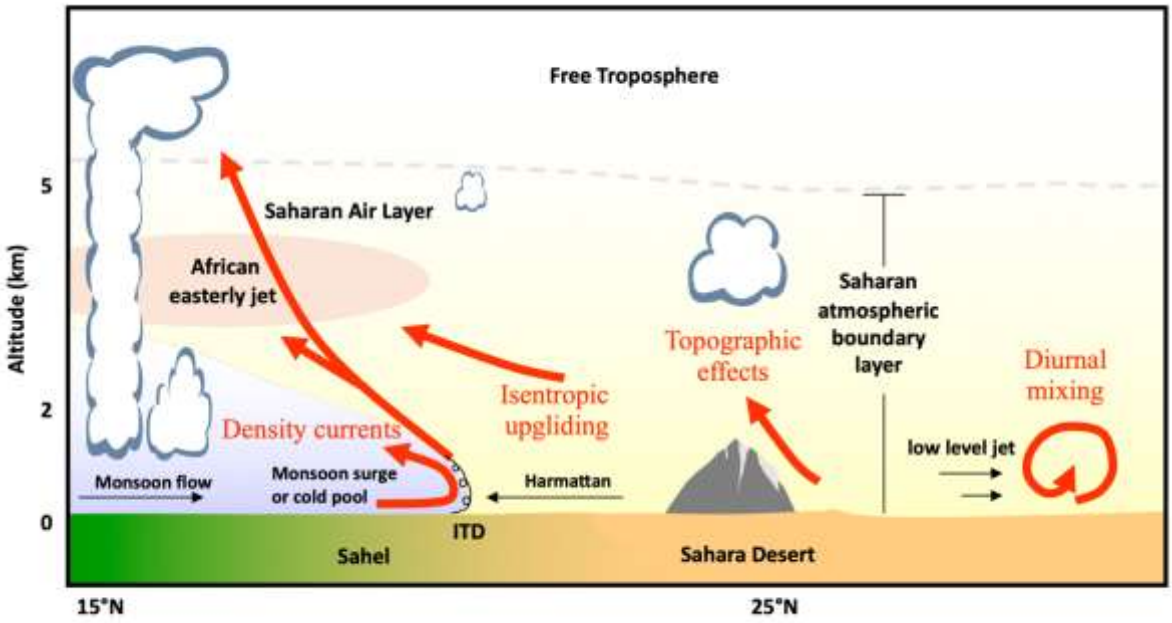

Figure 1. Schematic of mechanisms (red arrows) that control the vertical distribution of dust near the intertropical discontinuity (ITD): isentropic upgliding, cold pools, monsoon surges, topographic effects (e.g. orography) and diurnal vertical mixing of momentum from low-level jets. Shading (yellow or light blue) indicates air mass origins (i.e. respectively from the Saharan boundary layer or the Gulf of Guinea) and temperature. Mountains are found both north and south of the ITD. This illustration is adapted from Cuesta et al. (2009).

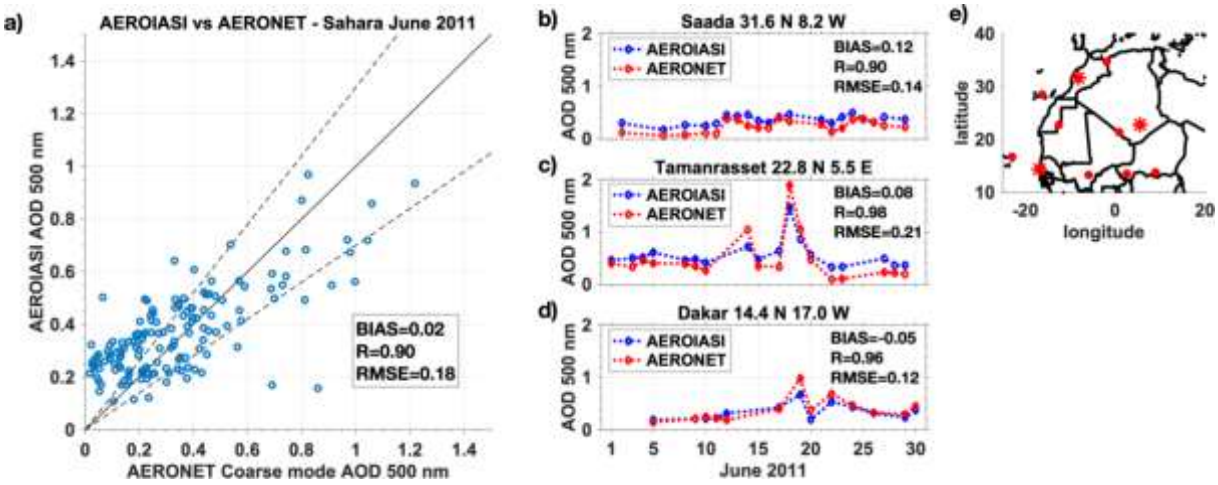

Figure 2. Comparison of dust optical depth at 500 nm derived from AEROIASI and AERONET sun photometers over the Sahara during June 2011. We use AOD extrapolated from the 10 µm spectral band to 500 nm for AEROIASI and the coarse mode fraction for AERONET. **(a)** Scatterplot for all AOD values derived for the 11 AERONET stations (Agoufou, Banizoumbou, Bordj Badji Mokhtar, Capo Verde, Cinzana, Dakar, Oujda, Saada, Tamanrasset, Tenerife and Zouerate) indicated in red in the map of panel **(e)** with quality checked retrievals from both AEROIASI and AERONET. Dashed black lines show the +/- 30 % with respect to the 1:1 line (plain black line). Time series of AOD for 3 stations (asterisks in panel e): **(b)** Saada in northern Africa, **(c)** Tamanrasset in the Central Sahara and **(d)** Dakar on the Atlantic coast southwest of the Sahara.

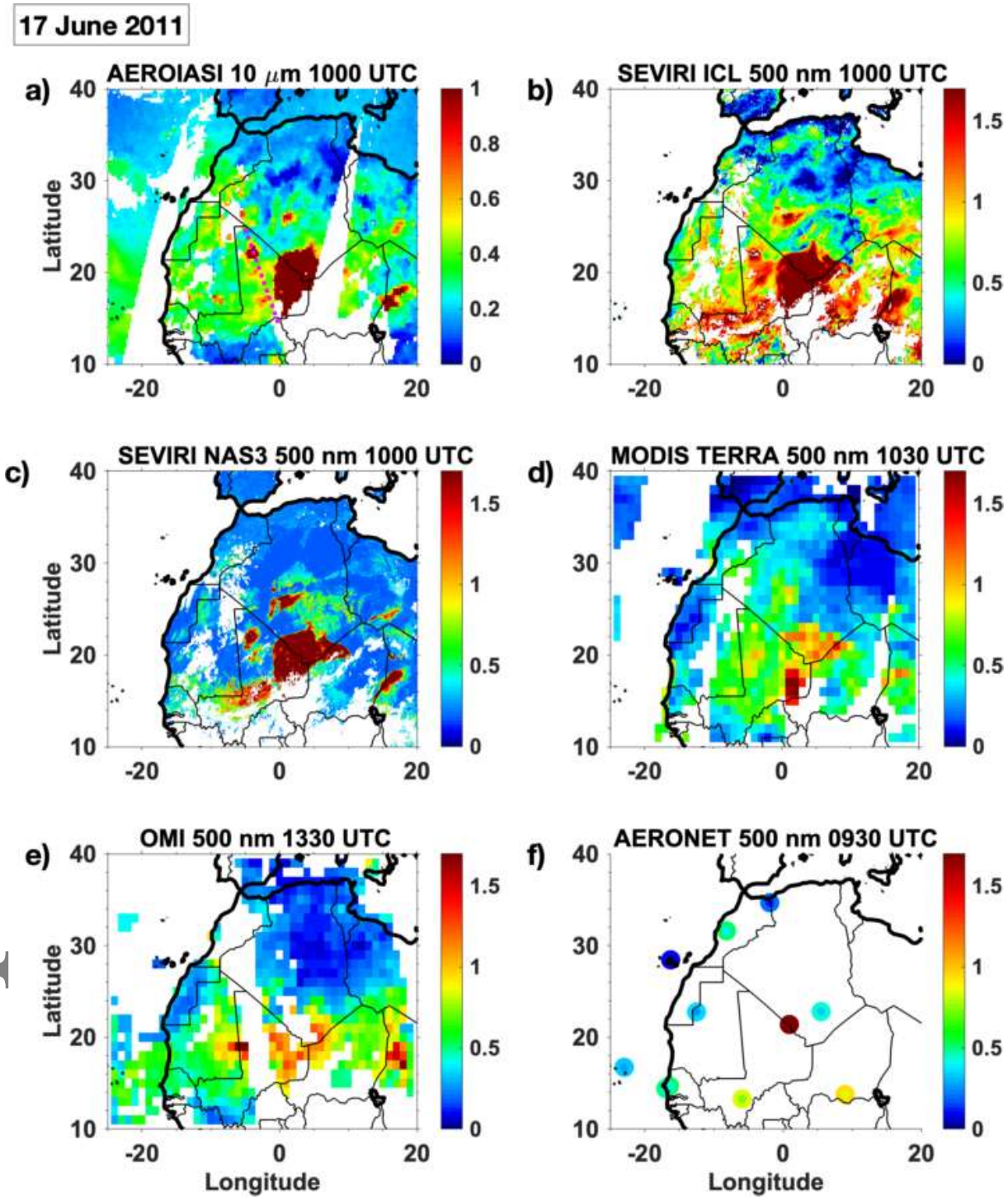

Figure 3. Comparison of dust optical depth over northern Africa on 17 June 2011 derived by **(a)** AEROIASI, **(b)** SEVIRI using the Imperial College London (ICL) approach, **(c)** SEVIRI using the North African Sand Storm Survey (NAS3) method, **(d)** MODIS onboard the TERRA satellite using the combined Dark Target/Deep Blue method, (e) OMI and (f) AERONET sun photometers. AEROIASI dust optical depth is estimated at 10 µm and other approaches at 500 nm. The difference in the colour scale (AEROIASI up to 1 and other products up to 1.7) accounts for the differences in wavelength. AERONET measurements are presented in small

circles for coarse mode aerosol optical depth, surrounded by larger circles showing all aerosol optical depth. The time of the measurement is shown in the title of each panel. The dashed magenta line in panel (a) is the CALIOP track of Figure 5a-b.

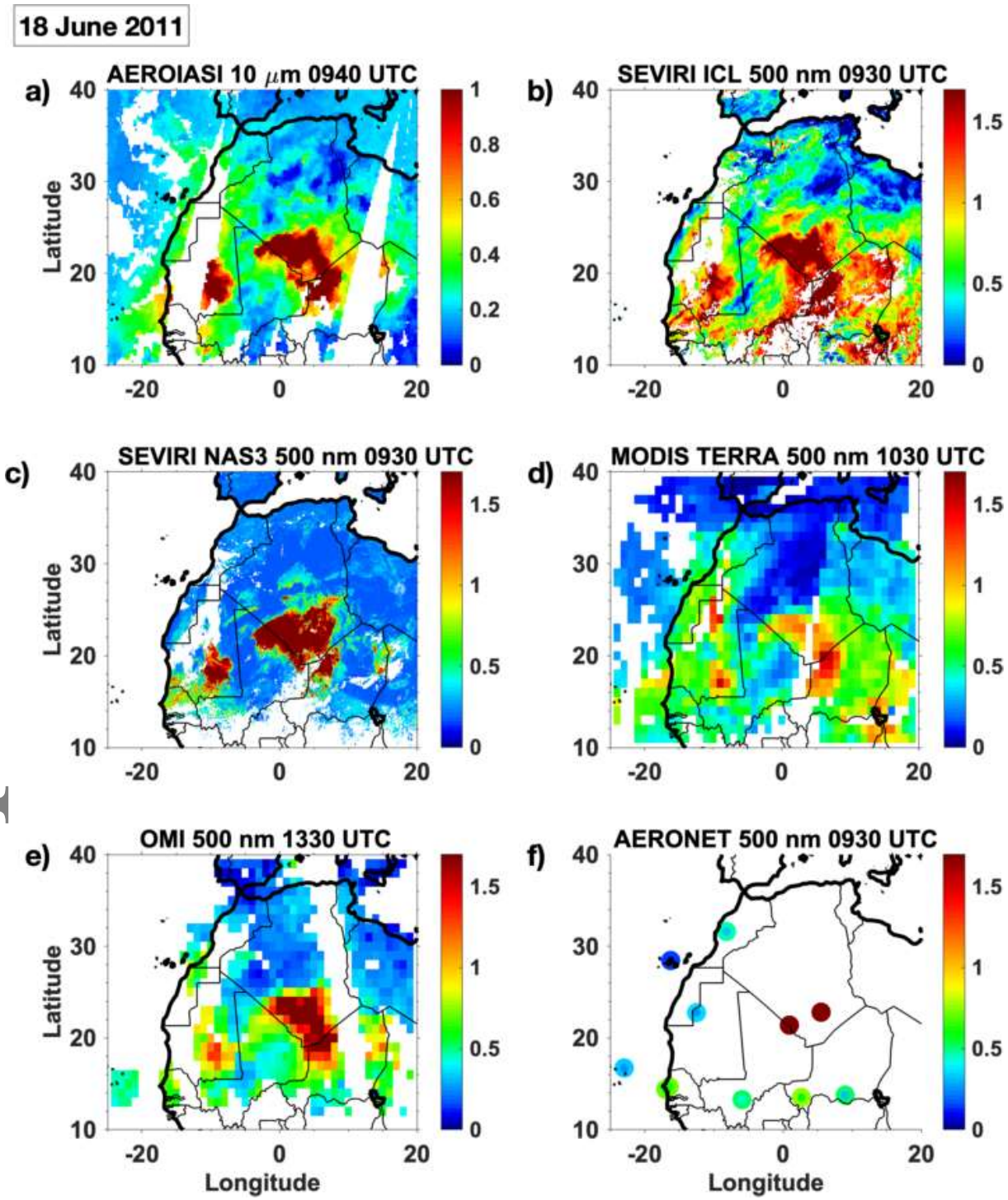

Figure 4. As Figure 3 but for 18 June 2011.

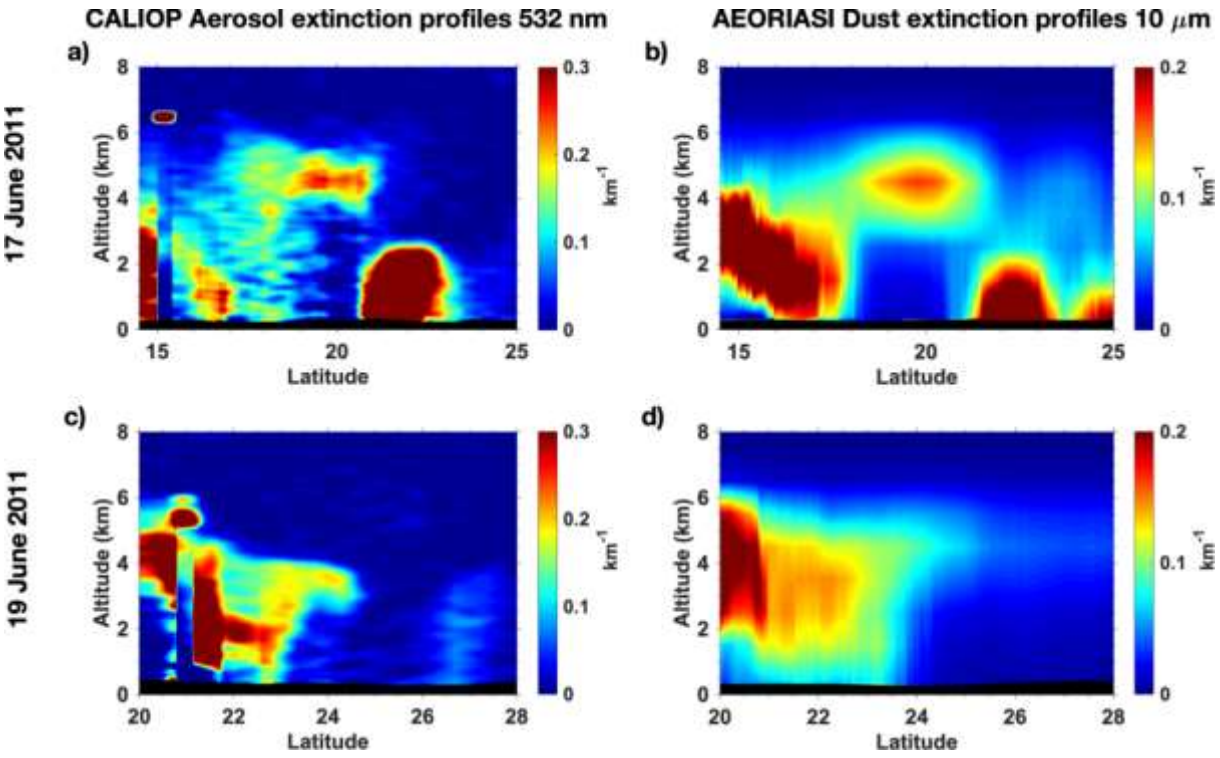

Figure 5. Vertical transects of aerosol extinction derived from **(left panels a, c)** CALIOP at 532 nm around 1300 UTC and **(right panels b, d)** AEROIASI at 10 µm around 1000 UTC, respectively on **(upper panels a, b)** 17 June 2011 and **(lower panels c, d)** 19 June 2011. For CALIOP, aerosol extinction is derived from attenuated backscatter measurements using a standard inversion approach and accounting for multiple scattering. For co-localisation between AEROIASI and CALIOP, AEROIASI data are sampled at the location of the airmasses observed by CALIOP approximately 3 hours later. High values of extinction at 6.5 km and 15°N (panel a) and 5.5 km and 21°N (panel c) of altitude for CALIOP are associated with the presence of clouds.

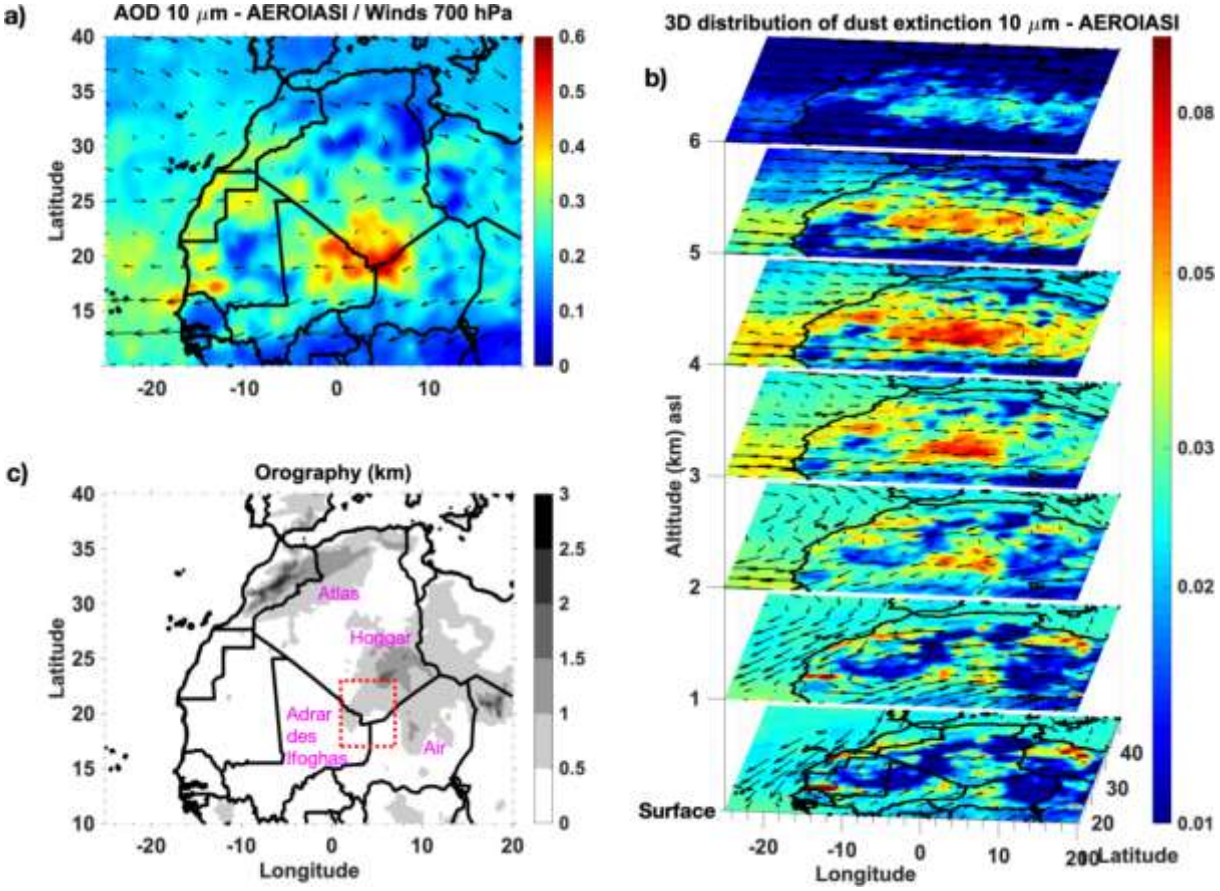

Figure 6. Monthly average of AEROIASI observations over northern Africa in June 2011: **(a)** Aerosol optical depth at 10 µm and **(b)** 3D distribution of dust in terms of extinction coefficient at 10 µm. Wind reanalysis fields from ERA5 at 700 hPa and at each level of the of the graph are overlaid on panels (a) and (b) respectively. Panel **(c)** shows orography of northern Africa and the dust hot spot in the central Sahara observed in June 2011 (red dashed area).

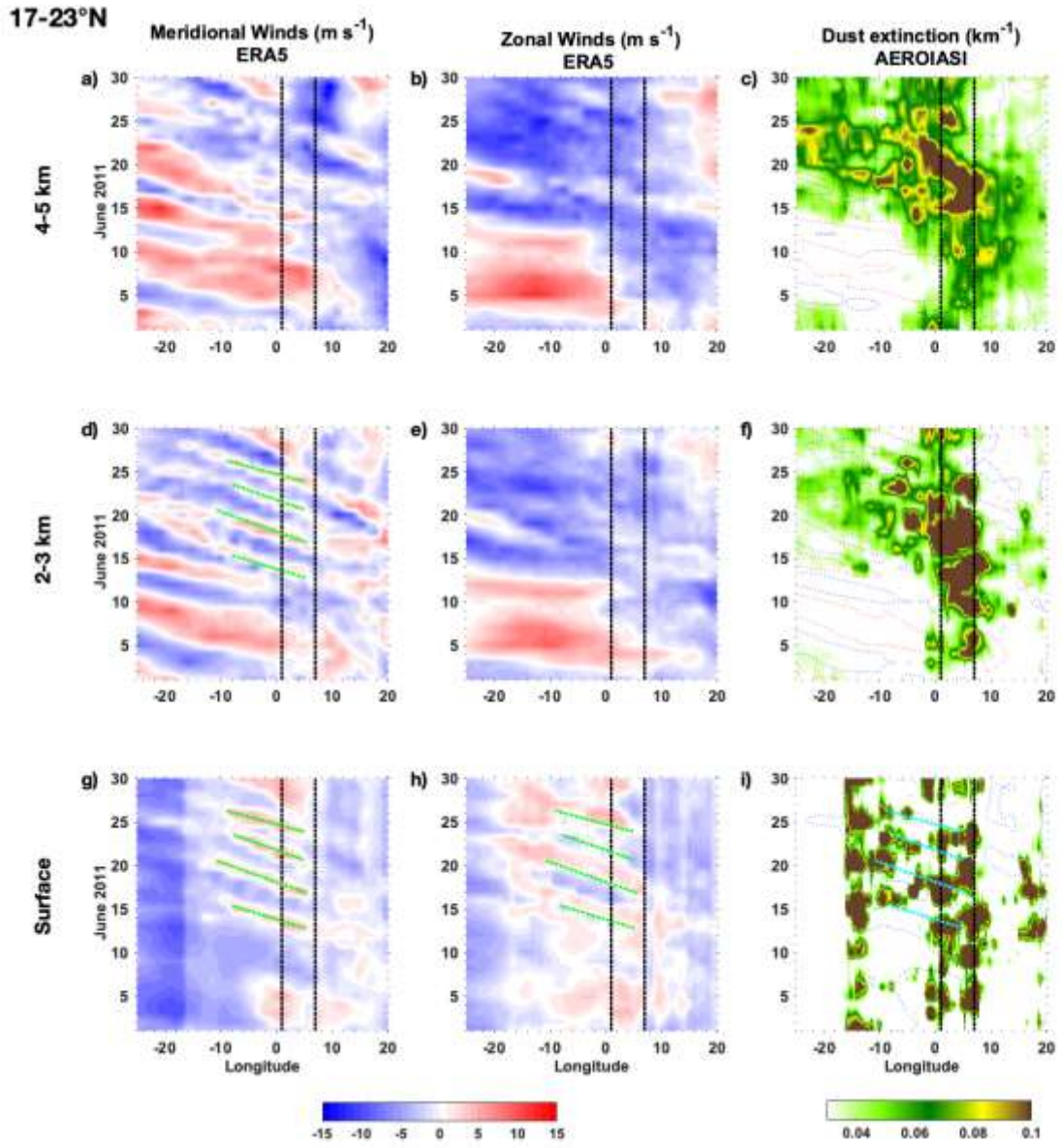

Figure 7. Hovmöller graphs of daily evolutions during June 2011 of **(left panels a, d, g)** meridional and **(middle panels b, e, h)** zonal wind from ERA5 and **(right panels c, f, i)** dust extinction observations at 10 µm derived from AEROIASI, averaged over the latitude band 17–23°N (the latitude of monthly AOD maximum). Different altitudes are shown: **(lower panels)** 10 m for wind and 0-1 km for dust**, (middle panels)** 2–3 km of altitude and **(upper panels)** 4–5 km of altitude**.** On the right panels, dashed contours of meridional winds of +/- 3 m s^{-1} (red/blue) are overlaid on dust extinction fields. Gaps in the AEROIASI time series for each geographical location are filled by interpolation between available data. Dotted black lines indicate the longitudinal band of the dust hot spot (1–7°E) and dotted green lines depict the 4 events of westward propagating southerlies at surface level initiating over the hot spot (the same lines are shown in panels d, h and i, in cyan for this last case).

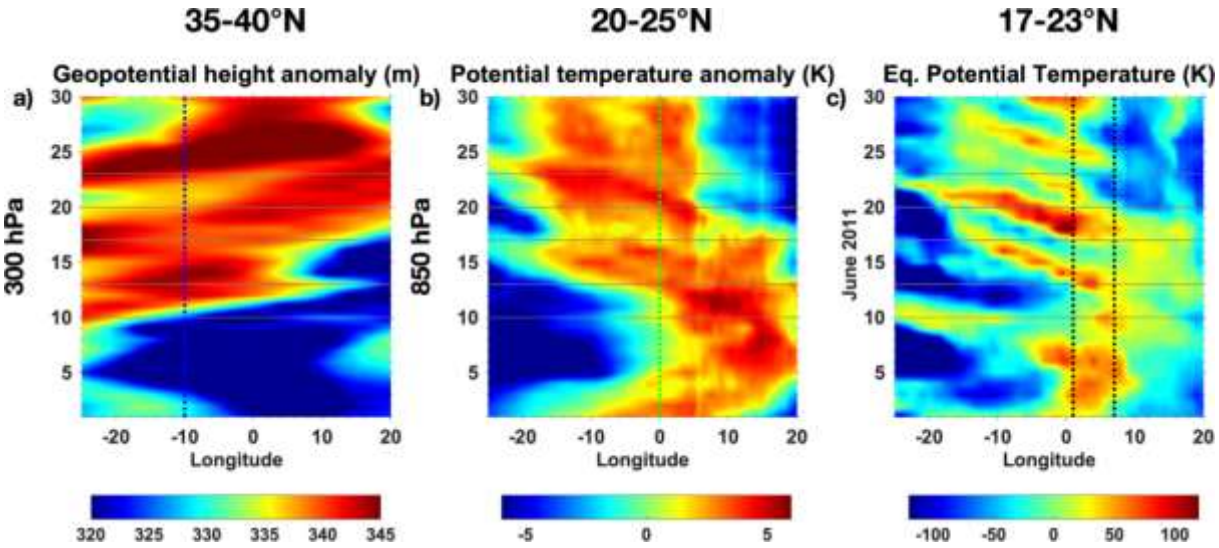

Figure 8. Hovmöller graphs of daily evolutions during June 2011 of: **(a)** geopotential height anomalies at 300 hPa for depicting the occurrence of extra-tropical (at 35–40°N) disturbances affecting the atmospheric circulation over the Sahara (particularly when located west of 10°W, blue dotted line), **(b)** potential temperature anomalies at 850 hPa and over 20–25°N used as a proxy to assess the longitudinal position of the SHL and its intensity and **(c)** equivalent potential temperature at 850 hPa over the latitude of the hot spot (17–23°N) to indicate the northward burst of the WAM (higher values correspond to monsoonal air masses). When the SHL position shifts west of 0°E (green dotted line), the associated cyclonic circulation favours the northward excursions of the WAM over the hot spot. Grey horizontal lines indicate the days of AOD peaks at the hot spot.

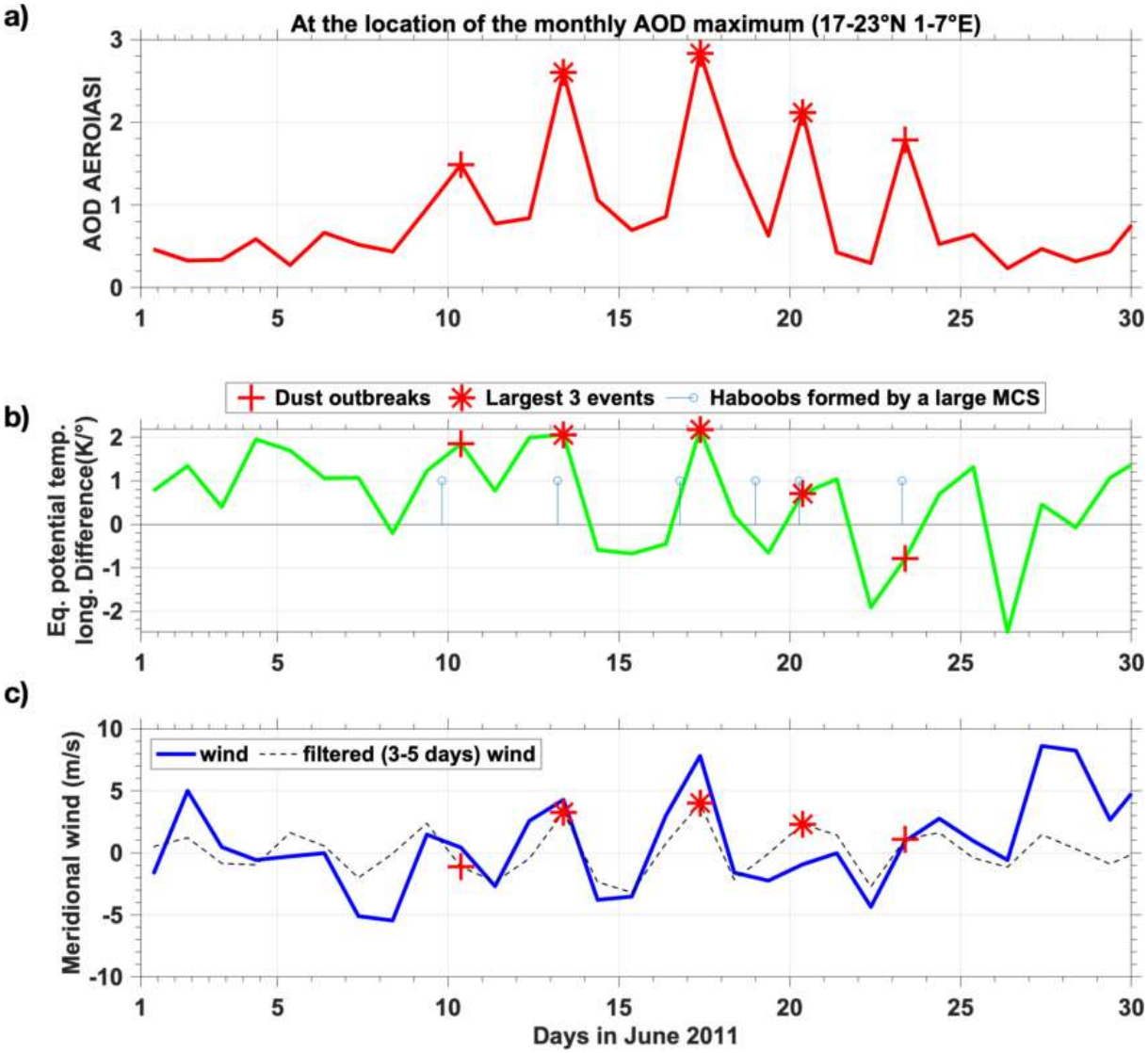

Figure 9. Daily evolution at the location of the monthly AOD maximum (17–23°N 1–7°E) over the Sahara in June 2011 of **(a)** dust optical depth at 10 µm derived from AEROIASI, **(b)** longitudinal difference of equivalent potential temperature at 850 hPa used as indicator of WAM northward excursions (green line) and occurrence of the formation of haboobs by MCSs larger than 5x5 ° and reaching the hot spot (blue stems, both haboobs and MCS tracked with SEVIRI observations as done in Fig. 10a and 12a) and **(c)** meridional winds at 850 hPa from ERA5 unfiltered (blue) and filtered (dotted black) for the 3–5 day variability associated with wave-like perturbations observed over the hot spot. Red asterisks indicate the days of the 3 dustiest events in concomitance with WAM bursts, cold pools and southerlies associated with waves red crosses for the other 2 significant dust peaks.

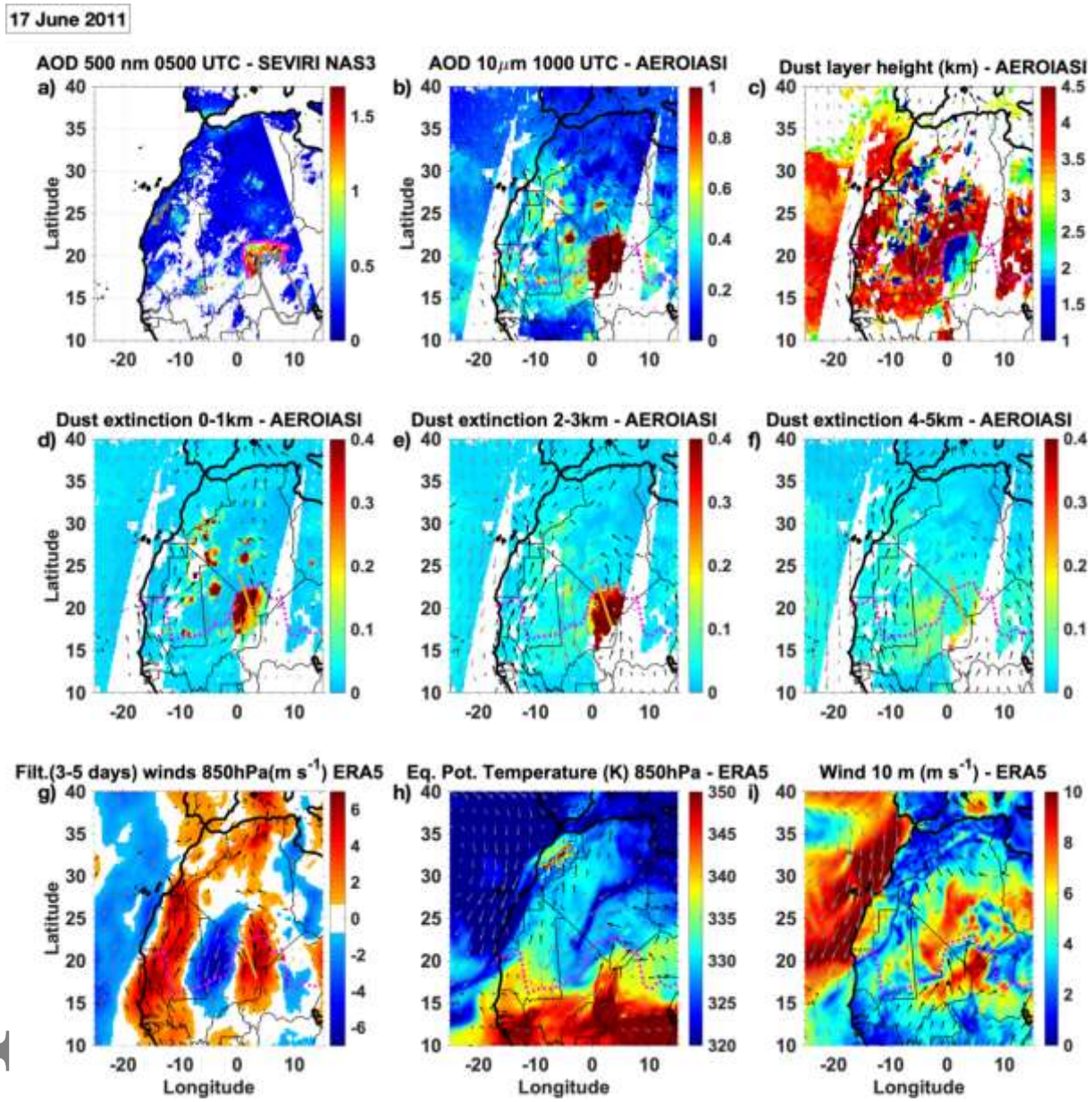

Figure 10. Characterisation of dust distribution and dynamical variables on 17 June 2011 over the Sahara. **(a)** AOD at 0500 UTC derived from SEVIRI NAS3, **(b)** AOD at 10 µm from AEROIASI at 1000 UTC, **(c)** Mean dust layer height (km) above ground level and dust extinction (km^{-1}) at 10 µm for the altitude **(d)** 0–1 km, **(e)** 2–3 km and **(f)** 4–5 km. ERA5 reanalysis at 0900 UTC of **(g)** filtered (3–5 days) winds at 850 hPa ($m\ s^{-1}$) shown with arrows (grey and black respectively with southward and northward components) and meridional windspeed (colours), **(h)** equivalent potential temperature at 850 hPa and **(i)** winds at 10 m above ground level. The grey and magenta plain lines in panel (a) show the location of respectively the MCS forming the haboob at 2100 UTC the previous day and the haboob at 0500 UTC. The magenta dotted line depicts the location of the ITD (surface wind changes north of the 15°C of dew point at 2 m, panels b–i). Arrows indicate winds in panel (h) and

filtered (3–5 days) winds in panels (b–g,i). The yellow line in panels (d-g) show the location of the vertical transect considered for the composite in Figure 11.

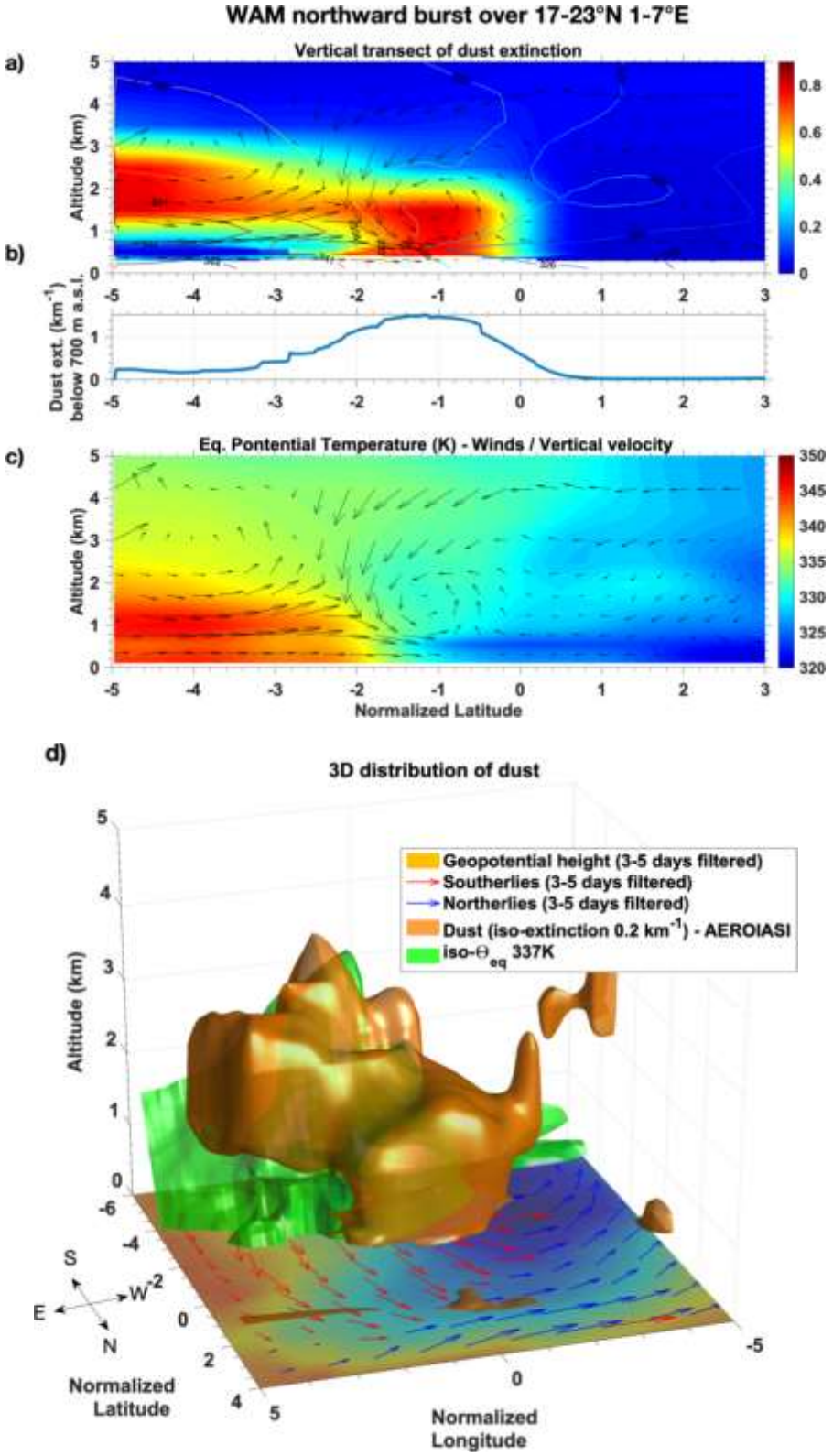

Figure 11. Composite the 3D distribution of dust and main dynamical variables describing the WAM and AEWs for the 3 main peaks of dust load over the Central Sahara, on the day of AOD maximum. Transects within the area of AEW southerlies co-located with the dust

plume of **(a)** dust vertical profiles and **(b)** dust extinction below 700 m a.s.l., both derived from AEROIASI, and **(c)** equivalent potential temperature (K), horizontal winds and vertical velocity from ERA5 projected on the transect. **(d)** 3D structures of the dust derived from AEROIASI and of the monsoonal air masses depicted by the 337 K isentrope of ERA5 reanalysis and the location of southerlies (red arrows), northerlies (blue arrows) and troughs (shading at surface level) associated with wave-like perturbations depicted by filtered (3-5 days) ERA5 winds and geopotential height anomalies, both at 850 hPa. Isentropes of equivalent potential temperature and projected winds are overlaid on the dust transect of panel (a). Averaging of the 3 cases (13, 17 and 20 June 2011) is done by prior normalisation of latitude and longitude, by considering 0° relative latitudes/longitudes as the location of the northward dust front within the southerlies of the wave-like perturbations.

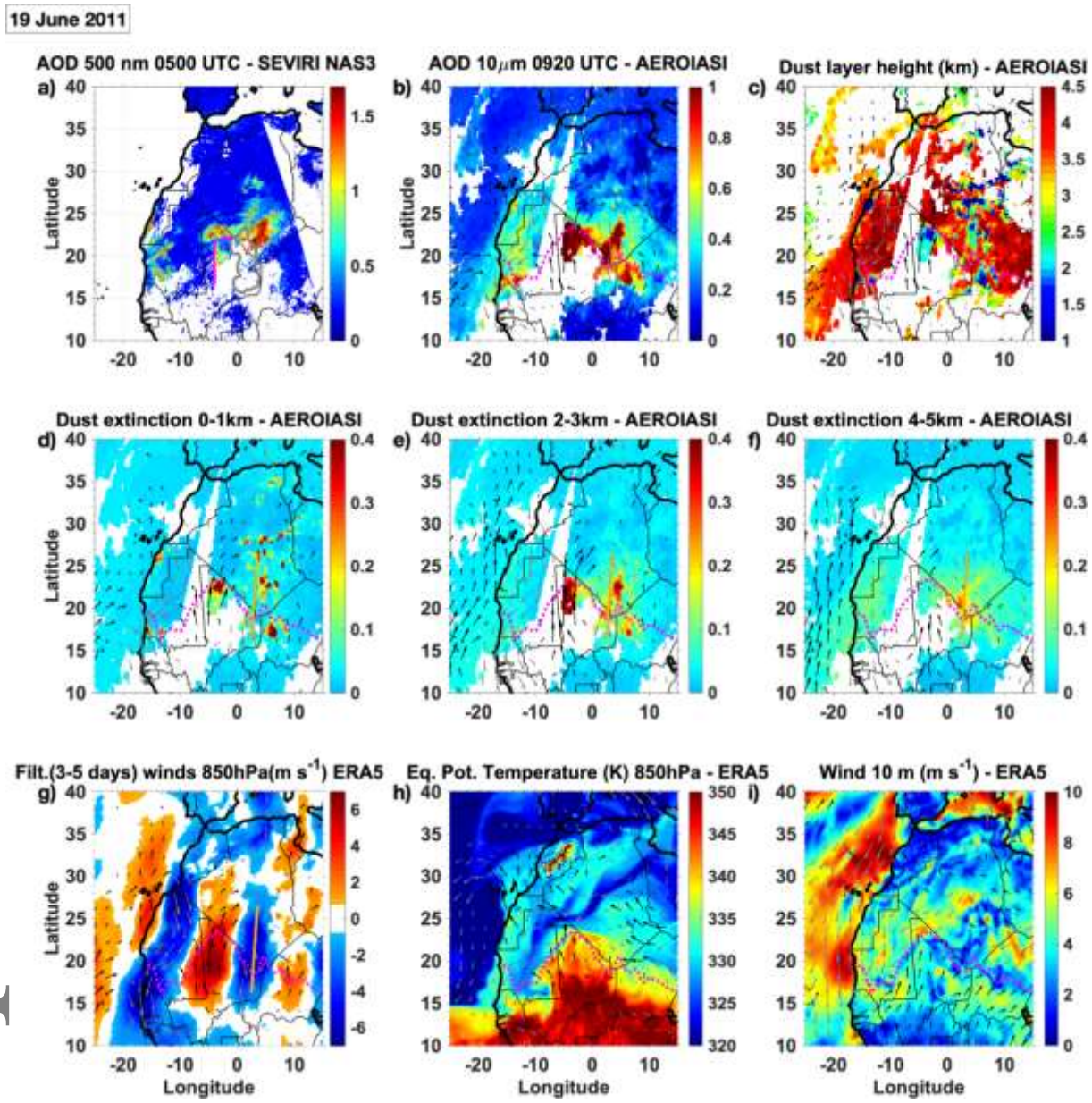

Figure 12. As Figure 10 but for 19 June 2011. AEROIASI retrievals are shown at 0920 UTC.

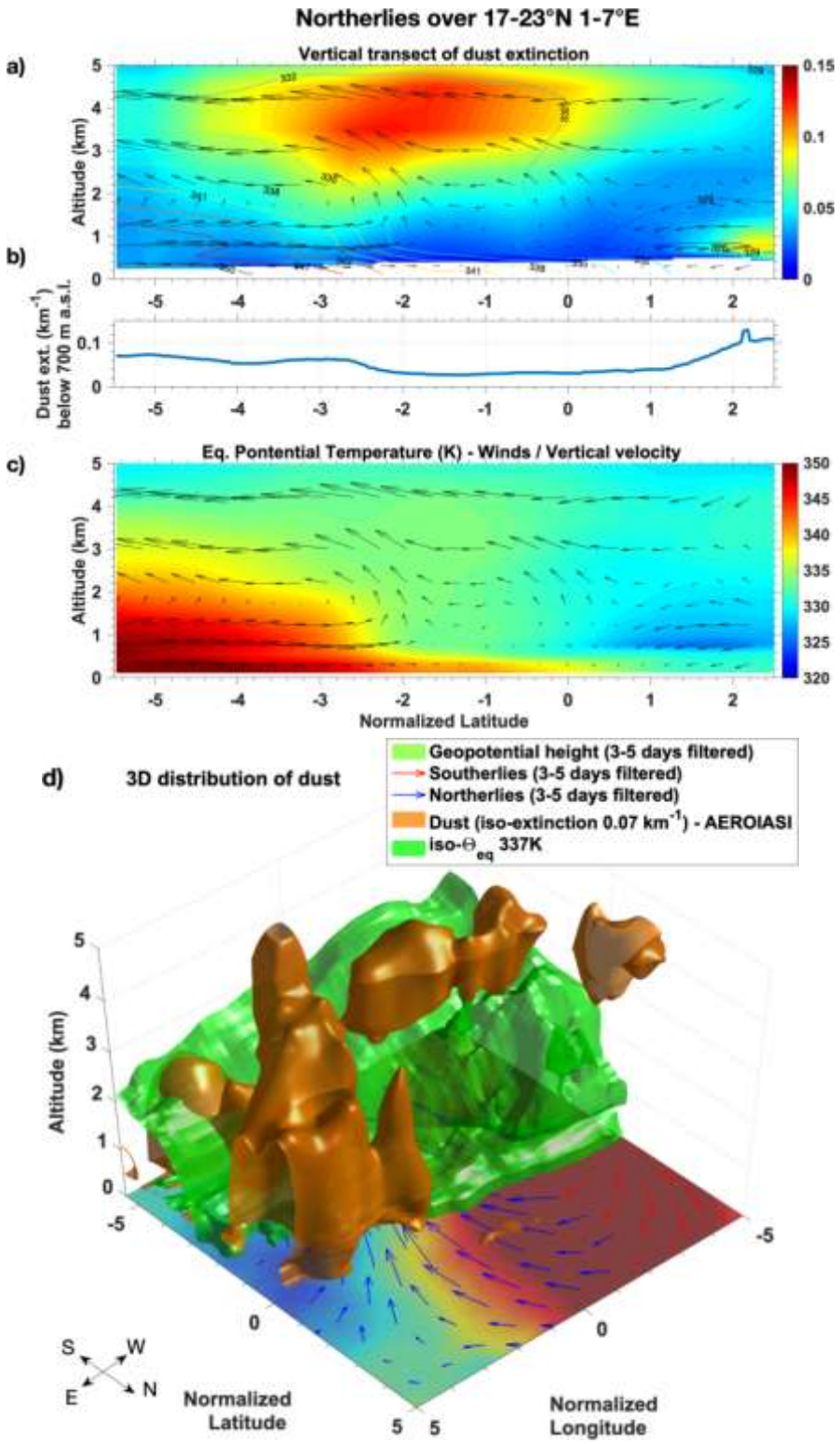

Figure 13. Same as Figure 11 but for composite dust and dynamical fields within the area northerlies associated with wave-like perturbations over the dust hot spot (17–23°N 1–7°E), occurring two days after the AOD maxima (i.e. 15, 19 and 22 June 2011).

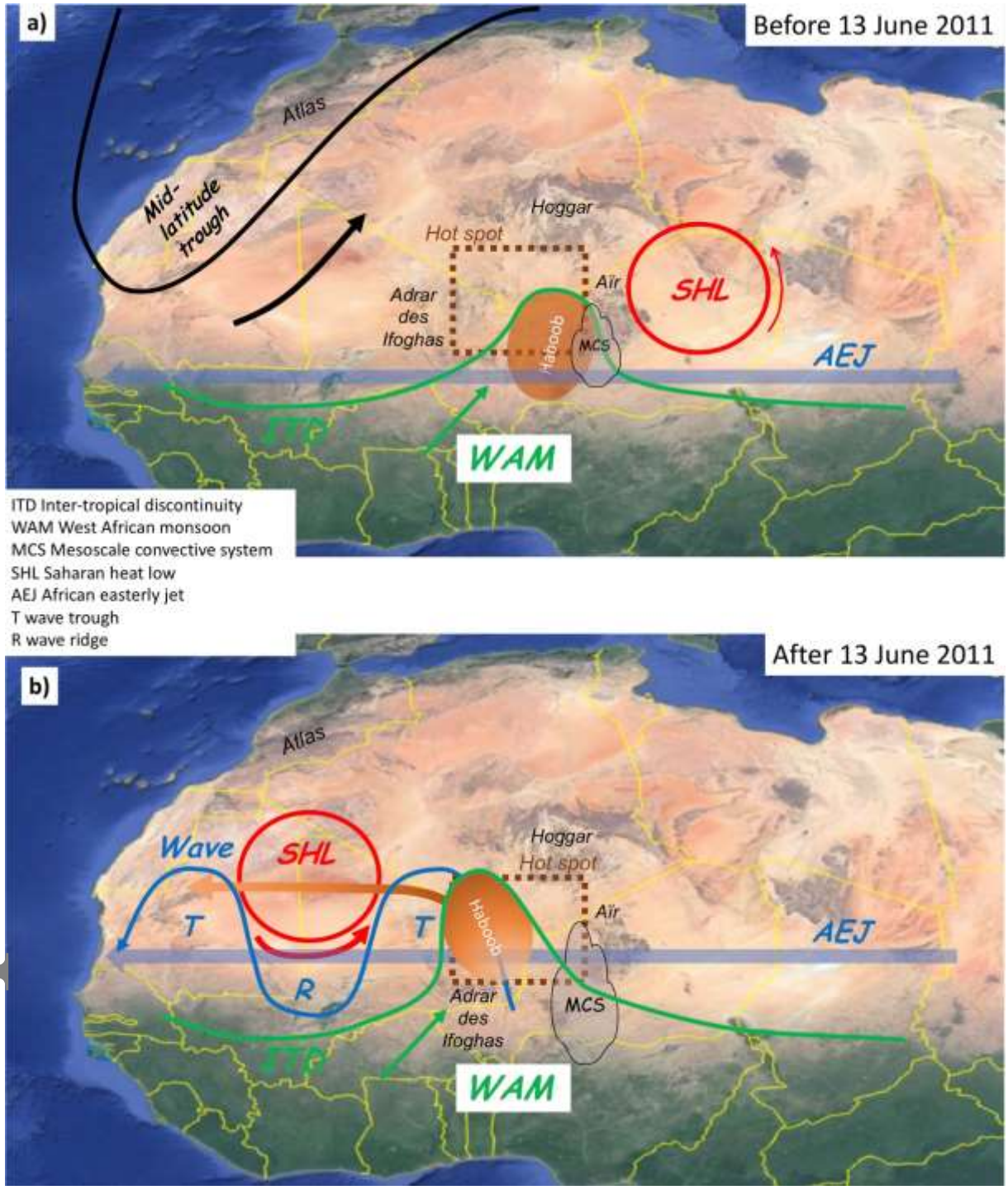

Figure 14. Schematic of the atmospheric dynamical conditions over West Africa leading to major dust emission over the central Sahara hot spot (17–23°N 1–7°E) during June 2011, **(a)** before and **(b)** after 13 June 2011. Brown shades indicate the location of the major dust plume emitted over the hot spot and its vertical distribution (darker and lighter brown for dust respectively extending from the surface to 2 km of altitude and above 2 km). The brown arrow show westward transport of dust by the AEJ.